

Abstract

Unresolved gravitational waves (GW) contribute to a stochastic GW background. This has not been measured yet using traditional GW detectors, like the Laser Interferometer Gravitational-Wave Observatory (LIGO), Virgo or the Kamioka Gravitational Wave Detector (KAGRA). With future detectors, such as Einstein Telescope (ET) or Cosmic Explorer (CE), the background is expected to be observed in the frequency range of about $10 - 10^3$ Hz. Its main contribution is expected to be of astrophysical origin. In this work, we will model the astrophysical gravitational wave background (AGWB) in a frequency-dependent way using an extension of the `Multi_CLASS` code. Through modification of this code, we compute angular power spectra of the AGWB that depend on frequency. We then assume the design noise of the cross-correlation between ET and CE to check whether the AGWB will be detectable. To achieve this, we use Information Field Theory (IFT) to separate our calculated power spectra from the design noise. The same method is also applied to the cosmological GW background. We find that it is possible to partly reconstruct the relatively high AGWB power spectrum at 400 Hz. However, even though future detectors are forecast to measure a large portion of GW events, we find that they will not be able to measure the AGWB at all frequencies or measure the cosmological background.

List of Abbreviations

AGWB	Astrophysical Gravitational Wave Background
BBH	Binary Black Hole
BH	Black Hole
CE	Cosmic Explorer
CLASS	Cosmic Linear Anisotropy Solving System
ET	Einstein Telescope
GW	Gravitational Wave
GWTC	Gravitational Wave Transient Catalogue
HMF	Halo Mass Function
IFT	Information Field Theory
KAGRA	Kamioka Gravitational Wave Detector
LIGO	Laser Interferometer Gravitational-Wave Observatory
LVK	LIGO, Virgo & KAGRA
NANOGrav	North American Nanohertz Observatory for Gravitational Waves
NIFTy	Numerical Information Field TheorY
SFR	Star Formation Rate

Contents

List of Abbreviations	ii
1 Introduction	1
2 Gravitational Waves	3
2.1 Fundamentals	3
2.1.1 Wave Equation	4
2.1.2 Free Field Modes	4
2.1.3 Quadrupole Wave Emission	6
2.1.4 Energy Flux	7
2.2 Stochastic Background	9
2.2.1 Astrophysical Component	10
Binary Black Hole Mergers	10
2.2.2 Cosmological Component	11
Inflation	12
2.2.3 Number Density Distribution	13
2.2.4 Projection Effects	14
3 Frequency Dependence of the AGWB	17
3.1 Energy Spectrum	18
3.2 Halo Mass Function	21
3.3 Star Formation Rate	24
3.4 Merger Rate	26
3.5 Window Function	27
3.6 Bias & Magnification Bias	30
3.7 Evolution Bias	31
4 Instrumental Noise	33
4.1 LIGO, Virgo & KAGRA	33
4.2 Einstein Telescope & Cosmic Explorer	34
5 Information Field Theory	36
5.1 Information Hamiltonian	36
5.2 Wiener Filter	37
5.3 1D Toy Model	38

6 Results	40
6.1 Frequency Dependent AGWB Angular Power Spectrum	40
6.2 AGWB vs. Noise	42
6.3 CGWB vs. Noise	48
7 Conclusion & Outlook	51
Acknowledgements	53
Bibliography	54
A Call Graph	58
List of Figures	60

1

Introduction

Most large-scale structure surveys, like Planck [Planck Collaboration et al. 2016], have found an unexpectedly large dipole anisotropy, which can be used to test the cosmological principle. The principle states that the universe is isotropic and homogeneous on large scales. These surveys have error sources, such as partial sky covering, due to masking sources and the fact that clustering of matter can produce an anisotropic contribution. GW have a very high sky coverage since masking is not necessary for GW detectors. Thus, we can use GW observations to test the cosmological principle in an independent way. This is possible because both tracers are related to the underlying matter distribution that was seeded in the early universe.

To do this, we can look at the AGWB. Many GW have an amplitude below the necessary signal-to-noise ratio to be detected individually. These sources form the GW background. Compact binary mergers are expected to make up the majority of this background in our considered frequency range of 1-1000 Hz. This background has been detected in a low-frequency range of $10^{-8.75} - 10^{-7.5}$ Hz in 2023 by the North American Nanohertz Observatory for Gravitational Waves (NANOGrav) pulsar time array with an energy density parameter of $\Omega_{GW} = 9.3_{-4.0}^{+5.8} \cdot 10^{-9}$ [Agazie et al. 2023]. In current GW experiments, like LIGO, Virgo and KAGRA (LVK), the noise is too high to detect this background. Experiments with a higher sensitivity are planned for the future, like the ground-based ET and CE. These might have low enough noise to detect the GW background and even disentangle different components. With these future detectors, we could possibly measure intrinsic anisotropies in this background which are not coming from our observer motion or statistical properties, i.e. shot noise from a Poisson distribution. A larger-than-expected intrinsic dipole or higher multipole would then contradict the cosmological principle.

We compute the anisotropies of the AGWB in a frequency-dependent way using a modified version of `Multi_CLASS` [Bellomo et al. 2020] which is based on `CLASS` [Blas, Lesgourgues, and Tram 2011], an Einstein-Boltzmann solver. The used code is publicly available ¹. It makes sense to use an Einstein-Boltzmann solver since the formalism of computing the AGWB angular power spectrum is similar to doing this for the cosmic microwave background.

In the next step, we model the noise using design sensitivities of ET+CE and

¹https://github.com/FelicitasKeil/Multi_CLASS

use a separation method from IFT on the AGWB at different frequencies, as well as on the cosmological GW background. Separating the intrinsic anisotropies of the background from noise would give us insight into the astrophysical parameters that govern this background and into the validity of the cosmological principle.

This thesis is structured as follows: In Chapter 2, we discuss the fundamental physics of GW and their stochastic background. Then, the frequency dependence of the AGWB is explained in Chapter 3. The instrumental noise of current and future experiments is presented in Chapter 4. IFT and the used techniques are summarised in Chapter 5. Then, we present the results in Chapter 6 before concluding and giving an outlook.

2

Gravitational Waves

2.1 Fundamentals

GW are oscillations in spacetime, similar to electromagnetic waves. We can treat them as small perturbations of the metric $g_{\mu\nu}$. To treat them analytically, this section follows Holten 2019 which considers only the inspiral phase of a compact binary merger. These mergers will be described below in section 2.2.1. To summarise shortly, the inspiral phase is the phase in which two heavy objects orbit around each other in a spiral form. They lose potential energy and convert it into GW, which we will see at the end of this calculation. We can derive the energy flux of the system in the inspiral phase using linear perturbation theory. Later, we will need the energy spectrum of a binary black hole (BH) in all three phases which will require corrections to this analytic approach. To do this, we start with the Einstein equation which relates the matter distribution to the spacetime curvature.

$$G_{\mu\nu} = \frac{8\pi G}{c^4} T_{\mu\nu} \quad (2.1)$$

Since GW (mostly) propagate in the vacuum and typically have small amplitude $|\delta g_{\mu\nu}| \ll 1$, we arrive at the following differential equation.

$$T_{\mu\nu} = 0 \quad (2.2)$$

$$\Rightarrow G_{\mu\nu} = 0 \quad (2.3)$$

We assume that the metric only has small linear perturbations $\delta g_{\mu\nu}$.

$$g_{\mu\nu}(t, \vec{x}) = \bar{g}_{\mu\nu} + \delta g_{\mu\nu}(t, \vec{x}) \quad (2.4)$$

$$= \eta_{\mu\nu} + 2\kappa h_{\mu\nu}(t, \vec{x}) \quad (2.5)$$

$$\kappa = \frac{\sqrt{8\pi G}}{c^2} \approx 2.1 \cdot 10^{-41} \frac{\text{s}^2}{\text{kg m}} \quad (2.6)$$

$$|h_{\mu\nu}| \ll 1 \quad (2.7)$$

Here $\eta_{\mu\nu}$ denotes the Minkowski metric for flat spacetime and $h_{\mu\nu}$ describes the perturbations from this background metric. The constant κ is defined in this way to

give $h_{\mu\nu}$ the standard dimensions of a bosonic tensor field, i.e. spin 1.

2.1.1 Wave Equation

If we want to describe the transport of energy and momentum by GW analytically, we can assume an asymptotically flat environment since the detector is at a far distance from the source. Then, we will consider Newtonian binaries in a circular orbit and only look at the non-relativistic regime. This will limit us to the inspiral phase, as mentioned above, since the non-relativistic approximation only applies in that phase. Later though, we will see that for a frequency dependence in our observables, all the phases need to be modelled.

The linear perturbation $h_{\mu\nu}$ is a dimensionless bosonic tensor field and thus follows the massless field equation:

$$\square h_{\mu\nu} - \partial_{\mu\nu}\partial^\lambda h_{\lambda\nu} - \partial_\nu\partial^\lambda h_{\lambda\mu} + \partial_\mu\partial_\nu h - \eta_{\mu\nu}(\square h - \partial^\kappa\partial^\lambda h_{\kappa\lambda}) = -\kappa T_{\mu\nu} \quad (2.8)$$

For the gauge transformation, we can impose the de Donder gauge condition:

$$\partial^\mu h_{\mu\nu} = \frac{1}{2}\partial_\nu h^\mu. \quad (2.9)$$

To simplify the wave equation we introduce the trace reverse tensor $\underline{h}_{\mu\nu}$.

$$\underline{h}_{\mu\nu} = h_{\mu\nu} - \frac{1}{2}\eta_{\mu\nu}h \quad (2.10)$$

Here, h is the trace of $h_{\mu\nu}$. With this, the wave equation reads:

$$\partial^\mu \underline{h}_{\mu\nu} = 0 \quad (2.11)$$

$$\Rightarrow \square \underline{h}_{\mu\nu} = -\kappa T_{\mu\nu}. \quad (2.12)$$

We can also choose h to be traceless, which leads to h and \underline{h} coinciding.

$$h = h^\mu_\mu := 0 \quad (2.13)$$

$$\Rightarrow \underline{h}_{\mu\nu} = h_{\mu\nu} \quad (2.14)$$

$$\Rightarrow \underline{h} = \underline{h}^\mu_\mu = 0 \quad (2.15)$$

2.1.2 Free Field Modes

Now, we can perform a Fourier decomposition of the linear perturbation.

$$\underline{h}_{\mu\nu}(x) = \int \frac{d^4 k}{(2\pi)^2} \epsilon_{\mu\nu}(k) e^{-ikx} \quad (2.16)$$

$$k = (\omega, \vec{k}) \quad (2.17)$$

The field equation is invariant under the following gauge transformation.

$$\epsilon'_{\mu\nu} = \epsilon_{\mu\nu} + k_\mu \alpha_\nu + k_\nu \alpha_\mu - \eta_{\mu\nu} k^\lambda \alpha_\lambda \quad (2.18)$$

Since k is the wave vector and GW propagate with the speed of light, it has to be a light-like four-vector.

$$k^2 = 0 \quad (2.19)$$

$$\Rightarrow \epsilon_{\mu\nu}(k) = e_{\mu\nu}(k)\delta(k^2) \quad (2.20)$$

To get a simplified amplitude form, we choose α from the gauge condition 2.18 in such a way that we eliminate e'_{00} , e'_{i0} and e'_{ii} .

$$\epsilon'_{\mu\nu}(k) = e'_{\mu\nu}(k)\delta(k^2) \quad (2.21)$$

For a wave propagating in z-direction, we will then get the following amplitude form.

$$e'_{\mu\nu}(\omega, \vec{k}) = \begin{pmatrix} 0 & 0 & 0 & 0 \\ 0 & e_+(\omega) & e_\times(\omega) & 0 \\ 0 & e_\times(\omega) & -e_+(\omega) & 0 \\ 0 & 0 & 0 & 0 \end{pmatrix} \quad (2.22)$$

We call e_+ and e_\times the plus and cross polarisations. To illustrate them, Fig. 2.1 shows both over one period.

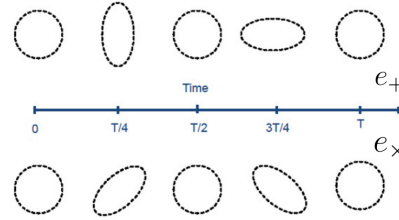


Figure 2.1: Illustration of the plus and cross polarisations varying with time. The figure is taken from an unpublished lecture by Prof. Jan van Holten, the author of Holten 2019.

Then, a plane wave in z-direction with only plus polarisation would have the following expression, since the cross polarisation will be zero.

$$h(z, t) = h_+ \begin{pmatrix} 0 & 0 & 0 & 0 \\ 0 & 1 & 0 & 0 \\ 0 & 0 & -1 & 0 \\ 0 & 0 & 0 & 0 \end{pmatrix} e^{i(kz - \omega t)} \quad (2.23)$$

A length of L_0 along the x-axis through which this GW passes would then oscillate in size in the following way:

$$L(t) = L_0 + \frac{h_+ L_0}{2} \cos(\omega t). \quad (2.24)$$

2.1.3 Quadrupole Wave Emission

We will now work in natural units, i.e. $c = 1$. If we have a source in a finite region of space, we can use the retarded Green's function to solve the wave equation. This is because the waves are causally related to the source $t > |\vec{x}' - \vec{x}|$.

$$\square \underline{h}_{\mu\nu} = -\kappa T_{\mu\nu} \quad (2.25)$$

$$\Rightarrow \underline{h}_{\mu\nu}(\vec{x}, t) = \frac{\kappa}{4\pi} \int d^3x' \frac{T_{\mu\nu}(\vec{x}', t - |\vec{x}' - \vec{x}|)}{|\vec{x}' - \vec{x}|} \quad (2.26)$$

Then, we can assume that we are in the far field regime, such that the observer $|\vec{x}|$ is far away from the source $|\vec{x}'|$.

$$|\vec{x}| \gg |\vec{x}'| \quad (2.27)$$

$$r := |\vec{x}| \approx |\vec{x}' - \vec{x}| \quad (2.28)$$

$$\Rightarrow \underline{h}_{\mu\nu}(\vec{x}, t) = \frac{\kappa}{4\pi r} \int d^3x' T_{\mu\nu}(\vec{x}', t - r) \quad (2.29)$$

If we consider a localised source, the solution does not have a dynamical time component, i.e. $\partial_0 h_{0j} = 0$. Additionally to the de Donder gauge (2.9), we will now impose the traceless-transverse gauge, which implies zero trace and transversality:

$$r_i \underline{h}_{ij} = 0 \quad (2.30)$$

$$\underline{h}_{ii} = 0 \quad (2.31)$$

If we consider which mass constellation can physically form GW, we could first imagine a dipole similar to a source for electromagnetic waves. However, a dipole would require a negative mass. The next possible multipole is then a quadrupole distribution, which is possible if we have two vacuum regions and two mass regions, like a binary black hole (BBH) for example. Here, each black hole (BH) is a massive region and the space between them is a vacuum region. For this reason, the GW strain depends principally on the quadrupole moment and does not have a dipole contribution. This gives us the following solution which is valid at a large distance in empty space. We use the unit vector of the distance between source and observer $\hat{r} = \vec{r}/|\vec{r}|$.

$$\underline{h}_{ij}(\vec{x}, t) = \frac{\kappa}{4\pi} (\delta_{ik} - \hat{r}_i \hat{r}_k)(\delta_{jl} - \hat{r}_j \hat{r}_l) \left(I_{kl} + \frac{1}{2} \delta_{kl} \vec{r} \cdot \vec{r} \right) \quad (2.32)$$

I_{ij} is the quadrupole moment of the total energy density:

$$I_{ij}(t - r) = \int d^3x' \left(T_{ij} - \frac{1}{3} \delta_{ij} T_{kk} \right) T_{00}(\vec{x}', t - r). \quad (2.33)$$

$$= \frac{1}{2} \partial_0^2 \int d^3x' \left(x'_i x'_j - \frac{1}{3} \delta_{ij} \vec{x}'^2 \right) T_{00}(\vec{x}', t-r). \quad (2.34)$$

The last equation follows since the time derivative is equal to the derivative with respect to the retarded time $u = t - r$.

$$\partial_0 = \partial_u \quad (2.35)$$

$$\Rightarrow \partial_0^2 T_{00}(\vec{x}', u) = \partial_0 \partial'_i T_{i0}(\vec{x}', u) = \partial'_i \partial'_j T_{ij}(\vec{x}', u) \quad (2.36)$$

As mentioned earlier, we can perform a non-relativistic approximation for the inspiral phase. In this case, the energy density is dominated by the mass density. We can thus rewrite \underline{h}_{ij} with the mass quadrupole moment.

$$I_{ij} = \frac{1}{2} \frac{\partial^2 Q_{ij}}{\partial t^2} \quad (2.37)$$

$$Q_{ij}(t-r) = \frac{1}{2} \int d^3x' \left(x'_i x'_j - \frac{1}{3} \delta_{ij} \vec{x}'^2 \right) \rho(\vec{x}', t-r) \quad (2.38)$$

The wave field for non-relativistic sources is thus:

$$\underline{h}_{ij}(\vec{x}, t) = \frac{\kappa}{8\pi} (\delta_{ik} - \hat{r}_i \hat{r}_k)(\delta_{jl} - \hat{r}_j \hat{r}_l) \frac{\partial^2}{\partial t^2} \left(Q_{kl} + \frac{1}{2} \delta_{kl} \vec{r} \cdot \vec{Q} \right) \quad (2.39)$$

2.1.4 Energy Flux

The energy in a certain volume changes with time depending on the divergence of the momentum flux Π integrated over the same volume.

$$\frac{dE_V}{dt} = - \int_V d^3x \nabla \cdot \Pi \quad (2.40)$$

The momentum flux depends on the time and space derivatives of $\underline{h}_{\mu\nu}$.

$$\Pi = -\nabla \underline{h}^{\mu\nu} \partial_t \underline{h}_{\mu\nu} \quad (2.41)$$

If we consider a plane wave in z-direction, we have the following strain, where $a, b \in [1, 2]$ and $h_{0i} = h_{3i} = 0$.

$$h_{ab} = e_{ab} \cos(\omega(t - z/c)) \quad (2.42)$$

$$e_{ab} = \begin{pmatrix} e_+ & e_\times \\ e_\times & -e_+ \end{pmatrix} \quad (2.43)$$

Then, we arrive at the time derivative of the energy flux per area at the z-coordinate 0.

$$\frac{dE}{dAdt} |_{z=0} = (\hat{n} \cdot \Pi) |_{z=0} \quad (2.44)$$

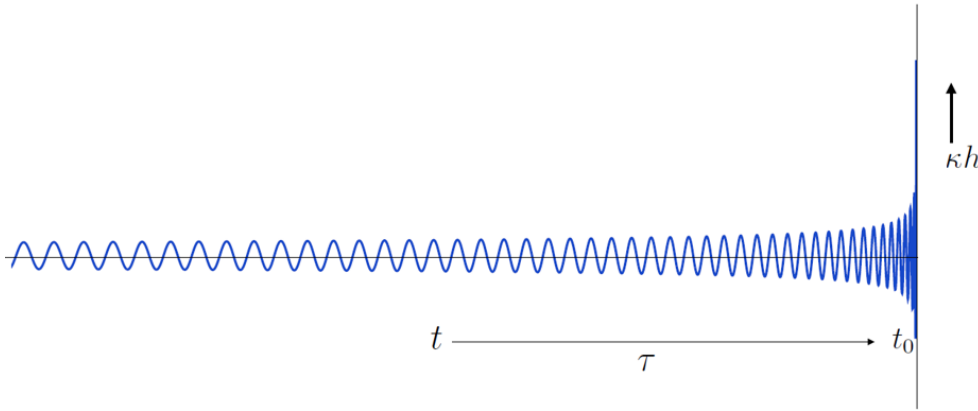


Figure 2.2: The GW inspiral phase waveform as described in this section. This figure is taken from an unpublished lecture of Prof. Jan van Holten, the author of Holten 2019.

$$= \partial_t h_{ab} \nabla_z h_{ab} |_{z=0} \quad (2.45)$$

$$= -\frac{2\omega^2}{c} (e_+^2 + e_\times^2) \sin^2(\omega t) \quad (2.46)$$

We can average this energy loss through GW over time. This is useful since we will also consider the stochastic background averaged over time. We consider the metric perturbations from the beginning for this expression.

$$a_{ij} = g_{ij} - \delta_{ij} = 2\kappa h_{ij} \quad (2.47)$$

$$\Rightarrow \left\langle \frac{dE}{dAdt} \right\rangle = \frac{\pi c^3 f^2}{8G} (a_+^2 + a_\times^2) \quad (2.48)$$

We will use a similar form of the GW energy but derived by the frequency later for computing the anisotropies. To do this, we need to calculate the rate of frequency change.

Without deriving this result, it is interesting to show the time dependence of the GW frequency. This depends on the chirp mass which is a combination of the two compact object masses and defines the waveform.

$$f(t) = \frac{c}{16\pi} \left(\frac{GM_c}{c^2} \right)^{-5/8} \left(\frac{5}{c(t_0 - t)} \right)^{3/8} \quad (2.49)$$

$$M_c = \frac{(m_1 m_2)^{3/5}}{(m_1 + m_2)^{1/5}} \quad (2.50)$$

Here, t_0 is the end of the inspiral phase. A waveform of the inspiral phase is shown in Fig. 2.2. In a higher-order description of GW, we find that we need other mass ratios for the waveform, see below (3.1).

2.2 Stochastic Background

The stochastic GW background consists of all sources that are too faint to be resolved individually, thus it is a superposition of many independent sources. The same source can contribute to multiple frequencies over time. The biggest background comes from astrophysical sources, like compact object mergers, but there is also a smaller cosmological background present. The latter originates from early universe phenomena.

In the following, we will use the more standard definition of $h_{\mu\nu}$ compared to Section 2.1 without the κ factor.

$$h_{\mu\nu} = g_{\mu\nu} - \eta_{\mu\nu} \quad (2.51)$$

To measure the background we need the correlation between two detector outputs (1,2) [Christensen 2019]. If the noise between them is uncorrelated, it will average out over time and leave the background signal.

$$\langle s_1(t)s_2(t) \rangle = \langle (n_1(t) + h(t))(n_2(t) + h(t)) \rangle \quad (2.52)$$

$$= \langle n_1(t)n_2(t) \rangle + \langle n_1(t)h(t) \rangle + \langle h(t)n_2(t) \rangle + \langle h(t)h(t) \rangle \quad (2.53)$$

$$\approx \langle h(t)h(t) \rangle \quad (2.54)$$

From there we can compute the root mean square of the strain.

$$h_{rms}^2 = \left\langle \sum_{i,j} h_{ij}h_{ij} \right\rangle \quad (2.55)$$

$$= \int_0^\infty df S_h(f) \quad (2.56)$$

Here S_h is the spectral density, from which we can derive the GW energy density.

$$\rho_{GW} = \int_0^\infty df S_h(f) \frac{\pi c^2 f^2}{8G} \quad (2.57)$$

The frequency-dependent monopole of the background Ω_{GW} depends on this energy density. Here, we consider the observed frequency f_o .

$$\bar{\Omega}_{GW}(f_o) = \frac{d\rho_{GW}}{df_o} \quad (2.58)$$

The energy density parameter is the frequency-dependent monopole integrated over the logarithmic frequency.

$$\Omega_{GW} = \int d \ln f \Omega_{GW}(f_o) \quad (2.59)$$

$$\approx \int d \ln f \bar{\Omega}_{AGWB}(f_o) \quad (2.60)$$

The current GW detectors, such as LVK, have not detected a GW background yet, but they have set upper limits from their third observing run [R. Abbott et al. 2021]. Assuming a GW energy density parameter proportional to $f^{-2/3}$, which is the case in the inspiral phase of BBH [Phinney 2001], they arrive at the following integrated energy density.

$$\Omega_{2/3,LIGO} \leq (3.4 \pm 6.1) \cdot 10^{-9} \quad (2.61)$$

This is compatible with zero, but an anisotropic background would indicate a more interesting cosmology, which is why it would be important to disentangle any anisotropies that could be observed.

The AGWB was detected for the first time this year (2023) using the pulsar time array NANOGrav [Agazie et al. 2023]. Pulsar time arrays use the fact that pulsars are very accurate clocks. They are rotating neutron stars that have a strong magnetic field and thus emit radio waves in very regular intervals. Since they are so stable, we can use these signals as clocks. If there are any changes in the time of arrival of multiple pulsars, this could indicate a GW background. The NANOGrav experiment used a frequency range of $10^{-8.75} - 10^{-7.5}$ Hz. Also assuming a frequency power law of $f^{-2/3}$, they find the following integrated energy density.

$$\Omega_{2/3,NANOGrav} = 9.3^{+5.8}_{-4.0} \cdot 10^{-9} \quad (2.62)$$

This is higher than the upper limit from LVK, but we have to keep in mind that the analysed frequency range is different for both experiments.

The contributions to this energy density are either of astrophysical or cosmological nature, but the former is expected to be some orders of magnitude larger than the latter.

2.2.1 Astrophysical Component

Considering astrophysical sources, GW they can be produced by merging binaries, bursts (e.g. from core-collapse supernovae) or continuous waves (e.g. from pulsars). The AGWB is dominated by compact object mergers which are mainly BH and neutron stars.

Binary Black Hole Mergers

A compact binary coalescence will produce a chirp-like GW signal, like in Fig. 2.4. Both massive objects attract each other and decrease their orbit around each other in the inspiral phase. The potential energy is converted into a GW. After the inspiral phase, the merger and ringdown phases follow, where the new BH becomes axisymmetric and stops emitting GW. The frequency increases over time during all three phases.

The inspiral phase is the simplest to describe analytically, see 2.1. However, in this work, we consider all three phases of the GW. We will see later that this is necessary to derive a frequency dependence.

In this work, we focus on BBH mergers since most resolved events from LIGO/Virgo are BBH. In a recent analysis of the Gravitational Wave Transient Catalogue 3 (GWTC-3) by The LIGO Scientific Collaboration et al. 2022, they considered events with a false alarm rate of less than $\frac{1}{4}$ per year. Out of this sample of 67 events, 63 came from BBH, 2 from binary neutron stars and 2 from neutron star-black hole mergers.

If we consider the energy density parameter of the stochastic GW background, we see that BBH are present at frequencies up to around 1000 Hz, see Fig. 2.3.

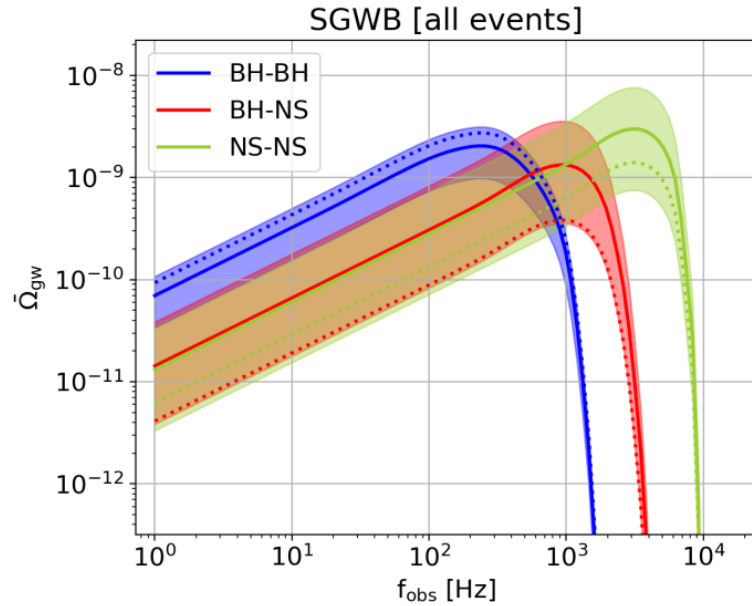


Figure 2.3: The GW energy density parameter as a function of frequency from 1 to 10,000 Hz. This shows the different contributions from BH-BH, NS-NS and BH-NS events. All curves are normalised to the local advanced LIGO/Virgo merger rate. The Figure is taken from Capurri et al. 2021.

In this figure, all three curves are normalised to the local merger rate from the advanced LIGO/Virgo detectors. Without this normalisation binary BH mergers dominate at most frequencies at which they are present. We can see that for the frequency range of 1 – 1000 Hz, it is reasonable to only consider BBH mergers in our analysis since they are the most present source. However, the applied formalism for the frequency dependence can be generalised to a system of a BH and a neutron star or a system of two neutron stars.

2.2.2 Cosmological Component

The major contributions to the cosmological GW background are primordial BH and GW from phase transitions and inflation. Schulze et al. 2023 computed the angular power spectrum of this background using a modified version of **CLASS** [Blas, Lesgourges, and Tram 2011] called **GW_CLASS**. GW from phase transitions arise when bubbles of a phase form in a universe which is still in an older phase. An everyday

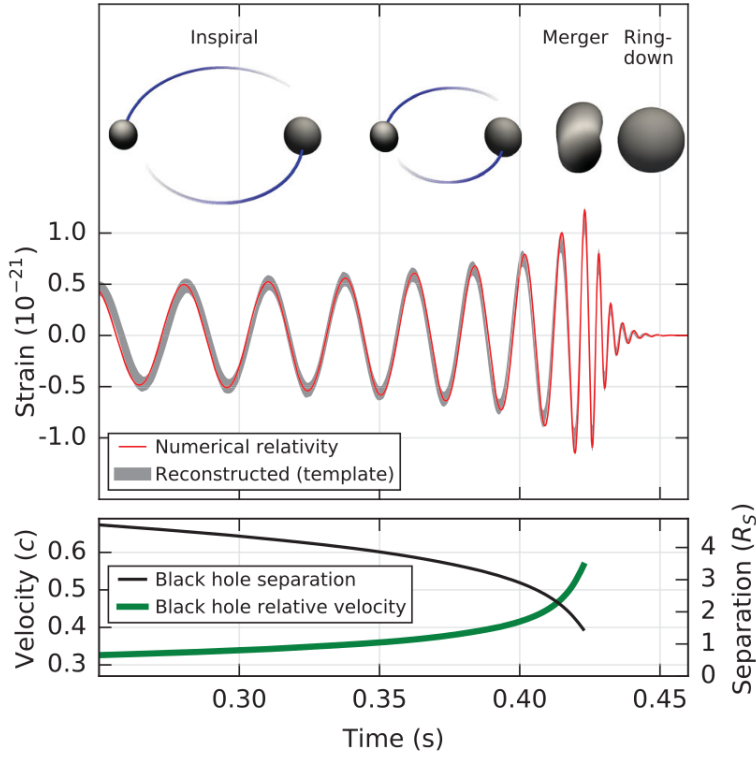


Figure 2.4: The different stages of a BBH merger with the corresponding waveform, here an illustrative estimate of GW150914. The Figure is taken from Ref. B. P. Abbott et al. 2016.

example of a first-order phase transition is boiling water. The entropy and the volume change discontinuously when going from one phase to another. In the early universe, first-order phase transitions could produce a cosmological GW background [Christensen 2019].

Primordial BH could have formed in the early universe during radiation domination. Since they are not produced from star formation, they can span a larger mass range than stellar BH.

In the `GW_CLASS` code, one can choose a source of this background, i.e. primordial BH, phase transitions or inflation, and compute the associated angular power spectrum. Here, we use the signal from the expected inflationary GW background with a blue tilt. So, we will have a stronger background at higher frequencies compared to lower frequencies.

Inflation

A period of inflation in the early universe solves two important cosmological problems, namely the flatness and the horizon problem. The flatness problem arises when we assume radiation domination followed by matter domination which is followed by Λ (the cosmological constant) domination. The spatial curvature density parameter is

measured to be very low.

$$|\Omega_k| = \frac{\rho_k^{\text{eff}}}{\rho_{\text{crit}}} < 10^{-2} \quad (2.63)$$

On the other hand, the radiation energy density parameter is of an even lower order.

$$|\Omega_r| = \frac{\rho_r}{\rho_{\text{crit}}} \in \mathcal{O}(10^{-4}) \quad (2.64)$$

Now the effective curvature energy density ρ_k^{eff} scales like a^{-2} , while the radiation energy density ρ_r scales like a^{-4} , with the scale factor a . At the Planck time $t_P = \sqrt{\frac{\hbar G}{c^5}}$ the ratio between them was many orders of magnitudes lower than 1.

$$\frac{|\rho_k^{\text{eff}}(t_P)|}{\rho_r(t_P)} \approx 10^{-62} \quad (2.65)$$

This seems unlikely since we would expect roughly the same order of magnitude for all the energy density parameters ρ_m , ρ_r , ρ_Λ , and ρ_k^{eff} . Random initial conditions would lead us to the same order of magnitude of these parameters. We also know how Ω_k scales with the scale factor.

$$\Omega_k = -\frac{k}{(aH)^2} = -\frac{k}{\dot{a}^2} \quad (2.66)$$

In the case of an inflationary GW background, the tensor power spectrum $P_T(k)$ creates the GW. This is linearly related to the average GW energy density parameter or monopole [Schulze et al. 2023].

$$\bar{\Omega}_{GW} = \frac{1}{12H_0^2 a_0^2} \frac{\eta_{eq}^2}{2\eta_0^4} P_T(k) \quad (2.67)$$

The GW created through large-scale perturbations during inflation are relevant for wavenumbers $k = 10^{-5} \text{Mpc}^{-1} - 1 \text{Mpc}^{-1}$, which corresponds to the millihertz up to the Hertz range, going through both the sensitivity range of ground-based detectors, like the upcoming ET [Alonso et al. 2020], and future space-based detectors like the Laser Interferometer Space Antenna or LISA [Robson, Cornish, and Liu 2019].

For a blue-tilted inflationary background, we need to choose an arbitrary cut-off frequency outside the sensitivity of the detector. Otherwise, this would overclose the universe at early times. We will assume this background later for the separation from ET+CE noise in the results chapter 6.

2.2.3 Number Density Distribution

To calculate the AGWB anisotropies, we need to assume a GW number density distribution with respect to redshift. Here, we use the `Multi_CLASS` code, an extension of the `CLASS` code by Bellomo et al. 2020. It was written to adapt the Einstein-Boltzmann solver to GW. In the computation of the source functions (section 2.2.4), it omits the Limber approximation. This approximation simplifies spherical Bessel

functions as Dirac distributions. The spherical Bessel functions are related to the ordinary Bessel functions in the following way.

$$j_n(x) = \sqrt{\frac{\pi}{2x}} J_{n+1/2}(x) \quad (2.68)$$

The ordinary Bessel functions are defined with the gamma function.

$$J_n(x) = \sum_{m=0}^{\infty} \frac{(-1)^m}{m! \Gamma(m+n+1)} \left(\frac{x}{2}\right)^{2m+n} \quad (2.69)$$

The `Multi_CLASS` code uses the number density of detectable GW per redshift per solid angle element from Scelfo et al. 2018:

$$\frac{d^2 N_{GW}}{dz d\Omega} = T_{obs} \frac{c \chi^2(z)}{(1+z) H(z)} R_{tot}(z) F_{GW}^{detectable}(z). \quad (2.70)$$

T_{obs} is the total observational time, $\chi(z)$ is the comoving distance, $H(z)$ is the Hubble rate, $R_{tot}(z)$ is the total comoving merger rate and $F_{GW}^{detectable}(z)$ the fraction of detectable events. For the merger rate, they include primordial BH and BBH in their calculation. The authors choose the common signal-to-noise threshold $\langle \rho^2 \rangle = 8$:

$$\langle \rho^2 \rangle = \frac{1}{5} \int_{f_{min}}^{f_{max}} df \frac{h_c^2(f)}{f^2 S_n(f)}. \quad (2.71)$$

The used frequency range is 10 – 10,000 Hz. S_n is the noise power spectral density and h_c is the characteristic strain.

$$h_c(f) = \frac{\sqrt{2}}{\pi \chi(z)} \sqrt{\frac{dE}{df_e}} \quad (2.72)$$

For ET, they find that $F_{GW}^{detectable} \approx 1$ even for redshifts above 5, which have a small effect on the detection overall.

2.2.4 Projection Effects

While GW travel towards us, they can be distorted by various effects. Mathematically, this comes through the integration along the line of sight. For the intrinsic anisotropies, there are four different contributions to the source functions Δ_l^{AGWB} . The different pertinent effects are density fluctuations, redshift space distortions, the Doppler effect and relativistic corrections or gravitational potential terms [Di Dio et al. 2013].

$$X(\eta, \vec{k}) = T_X(\eta, \vec{k}) \zeta(\vec{k}) \quad (2.73)$$

We write each random field as a product of the primordial curvature perturbation and a transfer function. Dall’Armi, Ricciardone, and Bertacca 2022 compute the different source terms using the `CLASSgal` framework. The implementation in `CLASS` follows the same framework, since `CLASSgal` has been merged into the standard

public code. The two-point correlation function of the curvature perturbation has the following form.

$$\langle \zeta(\vec{k})\zeta^*(\vec{k}') \rangle = (2\pi)^3 \delta(\vec{k} - \vec{k}') \frac{2\pi^2}{k^3} P(k) \quad (2.74)$$

Within the projection effects, there is one density source term, dependent on the transfer functions of matter density fluctuations $T_{\delta m}$ and of the velocity divergence of matter $T_{\theta m}$. Here, $\bar{\chi}$ is a shifted conformal time variable.

$$\bar{\chi} = \eta_0 - \eta \quad (2.75)$$

$$\Delta_\ell^{den} = \int_0^{\eta_0} d\eta W \left(bT_{\delta m} + 3 \frac{aH}{k^2} T_{\theta m} \right) j_l(k\bar{\chi}) \quad (2.76)$$

Here, $j_l(k\bar{\chi})$ is the spherical Bessel function and we integrate over conformal time using the window function, like in the following source contributions. b is the GW bias which will be treated in Section 3.6.

The Doppler terms also depend on the velocity divergence of matter since the velocity determines the Doppler effect.

$$\Delta_\ell^{D1} = \int_0^{\eta_0} d\eta W \frac{T_{\theta m}}{k} \left(-b_e + \frac{H'}{aH^2} + 3 \right) \frac{d}{d(k\bar{\chi})} j_l(k\bar{\chi}) \quad (2.77)$$

This depends on the evolution bias b_e which is frequency dependent in this formalism and will be discussed in Section 3.7. We need to model other frequency-dependent quantities, like the energy spectrum of a BBH merger, to compute it.

$$\Delta_\ell^{D2} = \int_0^{\eta_0} d\eta W T_{\theta m} (b_e - 3) \frac{aH}{k^2} j_l(k\bar{\chi}) \quad (2.78)$$

The term for the redshift space distortions was derived by Kaiser 1987 and depends on the second derivative of the bessel function.

$$\Delta_\ell^{RSD} = \int_0^{\eta_0} d\eta W T_{\theta m} \frac{1}{aH} \frac{d^2}{d(k\bar{\chi})^2} j_l(k\bar{\chi}) \quad (2.79)$$

There are five relativistic corrections, which can also be called gravitational potential terms since the redshift space distortions are also relativistic. In the GW case, two of these terms vanish [Dall’Armi, Ricciardone, and Bertacca 2022], while the other three are non-zero.

$$\Delta_\ell^{G1} = \int_0^{\eta_0} d\eta W T_\Psi \left(4 - b_e + \frac{H}{aH^2} \right) j_l(k\bar{\chi}) \quad (2.80)$$

$$\Delta_\ell^{G3} = \int_0^{\eta_0} d\eta W T_{\Phi'} \frac{1}{aH} j_l(k\bar{\chi}) \quad (2.81)$$

$$\Delta_\ell^{G5} = \int_0^{\eta_0} d\eta W \left(-b_e + \frac{H'}{aH^2} + 3 \right) \int_0^{\tilde{\eta}} d\tilde{\eta} j_l(k\bar{\chi}) \left(T_{\Phi'}(\tilde{\eta}) T_{\Psi'}(\tilde{\eta}) - \frac{1}{2} T'_{h,ij}(\tilde{\eta}) n^i n^j \right) \quad (2.82)$$

In the last equation, n^i are the components of the line of sight vector. All these effects are weighted with the window function to compute the GW density contrast, which will be discussed in Section 3.5.

3

Frequency Dependence of the AGWB

The AGWB is not independent of the observed frequency of the GW. In the standard `Multi_CLASS` code, it is possible to compute the angular power spectrum of the AGWB. However, this does not include any frequency dependency of this background which can generally not be neglected.

Therefore we added this frequency dependence which enters in two instances here. One is the frequency-dependent window function that weights contributions from different redshifts and the second is the evolution bias which accounts for new sources being added with time (i.e. lower z). Both will be discussed in Section 3.5 and 3.7.

To summarise in advance, the window function weights different redshift regions of the projection effects from Section 2.2.4 according to the source distribution.

$$\delta_{AGWB}(f_o, \hat{n}) = \int dz \tilde{W}(f_0, z) \Delta_{AGWB}(f_0, \hat{n}, z) \quad (3.1)$$

We need to specify the GW frequency as a parameter in the initialisation file that we give to `CLASS`, so we implemented it as a new input parameter for `Multi_CLASS`.

The frequency dependence of the window function is only present if we consider not only the inspiral phase but also the merger and ringdown phases. For the inspiral phase, we would have the following energy spectrum.

$$\frac{dE_{GW}}{df_e d\Omega_e} \propto f_0^{-\frac{1}{3}} (1+z)^{-\frac{1}{3}}. \quad (3.2)$$

$$\bar{\Omega}_{AGWB} \propto f_0^{\frac{2}{3}} \quad (3.3)$$

Considering only the inspiral phase would then make the window function frequency independent.

$$\tilde{W}(z) \propto \frac{f_0(dE_{GW}/df_e d\Omega_e)}{\bar{\Omega}_{AGWB}(f_0)} = const. \quad (3.4)$$

For that reason, it is necessary to consider all three phases of the merger which we will see in the energy spectrum, see also Fig. 3.1. Since the window function depends on the rate of BBH mergers and on the energy spectrum of one individual merger, we need to model these two components. How this is realised in the code

can be seen on the call graph in the Appendix A.

Section 3.1 and 3.4 discuss the frequency dependence of the energy spectrum and the merger rate, respectively. For the merger rate, we need to model the star formation rate (SFR) and the halo mass function (HMF) which is done in Sections 3.3 and 3.2. The resulting window function is shown in Section 3.5. GW biases are treated in Sections 3.6 and 3.7.

3.1 Energy Spectrum

For the modelling of all three phases of the binary coalescence we use the waveform by Ajith et al. 2011. The phases are inspiral, merger and ringdown, as shown schematically in Fig. 3.1. They arrive at this expression using post-Newtonian corrections to more standard waveforms. This is done in geometric units, i.e. $G = c = 1$.

$$A(f) = Cf_1^{-7/6} \begin{cases} f'^{-7/6}(1 + \sum_{i=2}^3 \alpha_i v^i) & f < f_1 \\ \omega_m f'^{-2/3}(1 + \sum_{i=1}^2 \epsilon_i v^i) & f_1 \leq f < f_2 \\ \omega_r \mathcal{L}(f, f_2, \sigma) & f_2 \leq f < f_3 \end{cases}$$

Note that this is the amplitude as a function of the frequency, so a Fourier transform of $A(t)$. Here, f' is a frequency ratio using the first transition frequency, see below.

$$f' = \frac{f}{f_1} \quad (3.5)$$

The parameter ν is dimensionless since we are working in geometric units.

$$\nu = (\pi M f)^{1/3} \quad (3.6)$$

The parameters ω_m and ω_r are used to make the function continuous and thus are dependent on the total mass $M = m_1 + m_2$. The parameters α_i are post-Newtonian corrections. They are calculated using general relativity and their values are shown in Table 3.1 along with the values for ϵ_i . Depending on the symmetric mass ratio η and the spin parameter χ , they take different values. The values are given with and without the zero-spin approximation which is used in this work.

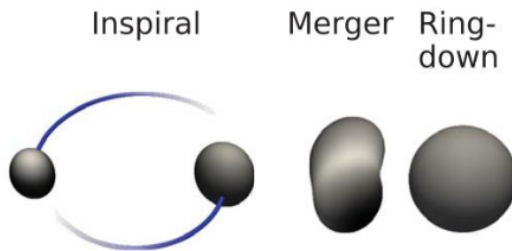


Figure 3.1: The three phases of a binary coalescence: inspiral, merger and ringdown.

$$\eta = \frac{m_1 m_2}{M^2} \quad (3.7)$$

$$\chi = (1 + \delta) \frac{\chi_1}{2} + (1 - \delta) \frac{\chi_2}{2} \quad (3.8)$$

Here, δ is the mass difference and χ_i depends on the spin angular momentum S_i of the i th BH.

$$\delta = \frac{m_1 - m_2}{M} \quad (3.9)$$

$$\chi_i = \frac{S_i}{m_i^2} \quad (3.10)$$

Parameter	α_2	α_3	ϵ_1	ϵ_2
Value	$-323/224 + 451\eta/168$	$(27/8-11\eta/6)\chi$	$1.455\chi-1.890$	$-1.815\chi + 1.656$
No Spin	$-323/224 + 451\eta/168$	0	-1.890	1.656

Table 3.1: Amplitude parameters with and without the zero spin approximation.

The frequency f_1 at the transition of the inspiral and merger phase is the last stable orbit of the binary. Once the merger phase has started the orbits cease to be stable since the objects start to fall in. This corresponds to a maximum of the effective potential. The frequency was calculated by Bardeen, Press, and Teukolsky 1972.

$$f_1 = \frac{c^3}{6^{3/2} 2\pi M G} \quad (3.11)$$

The transition frequency from merger to ringdown is given by the least-damped mode [Maggiore 2008] which is also the dominant quasi-normal mode. This is part of the description of the BBH system as characterised by n normal modes with frequencies ω_n , discussed further in chapter 12.3 of the same book.

$$f_2 \approx 0.747 \frac{c}{2\pi R_S} \approx 12 \text{kHz} \left(\frac{M_\odot}{M} \right) \quad (3.12)$$

For the ringdown, we have a Lorentzian function \mathcal{L} centred around the merger to ringdown transition frequency f_2 with the width σ .

The global normalisation factor C has the following form in SI units.

$$C = \sqrt{\frac{5}{24}} \frac{(GM_c)^{5/6}}{\pi^{2/3} c^{3/2}} \frac{(1+z)^2}{d_L} \quad (3.13)$$

This depends on the chirp mass which characterises a waveform instead of the total mass and the luminosity distance.

$$M_c = \frac{(m_1 m_2)^{3/5}}{(m_1 + m_2)^{1/5}} \quad (3.14)$$

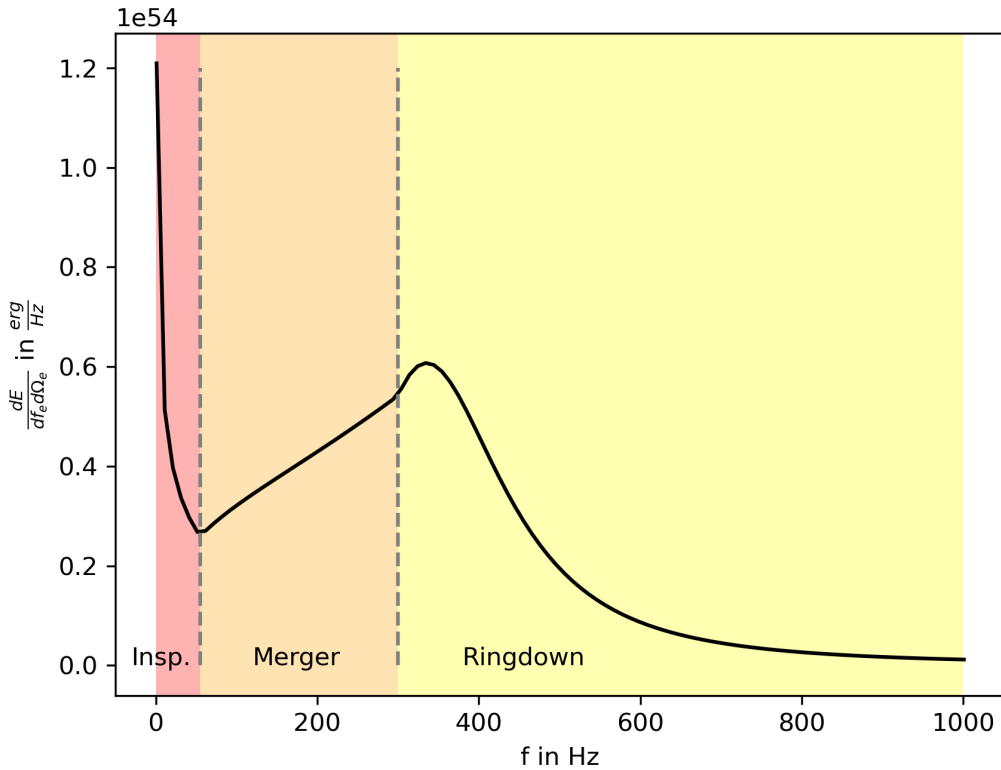


Figure 3.2: The energy spectrum as a function of the observed frequency for a BBH merger where both BH have a mass of $20M_\odot$ at $z = 0$.

$$d_L = a_0(1+z) \int_0^z d\tilde{z} \frac{c}{a_0 H(\tilde{z})} \quad (3.15)$$

The strain is directly given by the amplitude and a phase $\psi(f)$.

$$h(f) = A(f)e^{-i\psi(f)} \quad (3.16)$$

Later, we will consider the square strain as a function of frequency $|h(f)|^2 = |A(f)|^2$ for the energy spectrum, so we can omit the phase $\psi(f)$. Here, the redshift dependence will enter later through the derivation by the emission frequency. From this waveform template, we can get the energy spectrum in the following way.

$$\frac{dE_{GW,e}}{df_e d\Omega_e} = \frac{\pi d_L^2 c^3 f_o^2}{2G(1+z)^2} |h(f_o)|^2 \propto f_o^2 h^2(f_o) \propto h^2(t) \quad (3.17)$$

We show the energy spectrum as a function of z for different frequencies, see Fig. 3.3, again for two BH with a mass of $20M_\odot$ each. We can see different sections of Fig. 3.2 here. This is because $dE_{GW,e}/df_e d\Omega_e$ only depends on z through the emitted frequency. The energy spectrum is written as a function of f_e , but we implement it in such a way that the user can choose the received frequency at the detector.

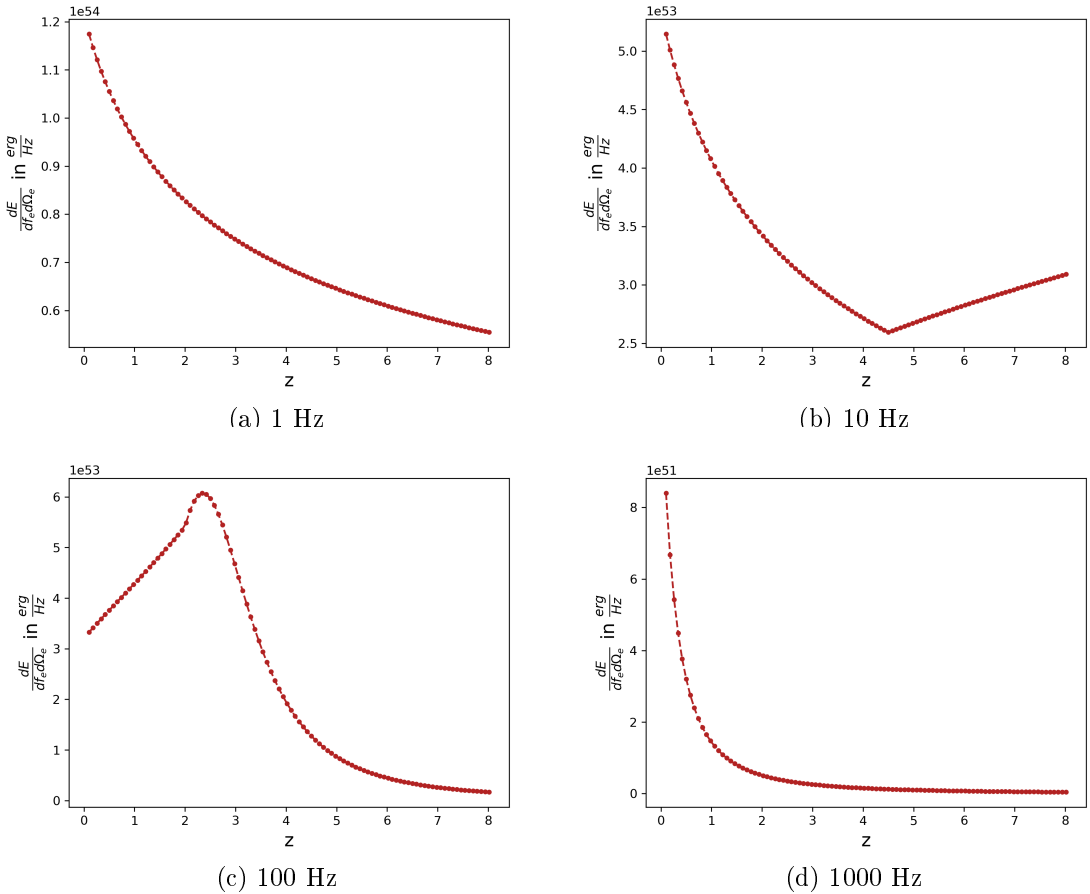


Figure 3.3: The energy spectrum $dE_{GW,e}/df_e d\Omega_e$ at different observed frequencies as a function of redshift, again for two BH with a mass of $20M_\odot$ each.

$$f_e = (1 + z)f_0 \quad (3.18)$$

At lower frequencies, like 1 Hz, the energy spectrum consists of the inspiral phase. At 10 Hz, we can see the transition from the inspiral to the merger phase. The transitions are not always smooth since the parameters ω_i fix the continuity of the curve but not the slope. The transition to the ringdown is visible at 100 Hz. At high frequencies such as 1000 Hz, the ringdown phase dominates at all redshifts.

The BH masses follow a probability distribution over which we would need to integrate separately. However, to speed up the calculation in our code, we assume $m_1 = m_2 = 20M_\odot$. This is a common BH mass considering GW observations from LVK [The LIGO Scientific Collaboration et al. 2022.]

3.2 Halo Mass Function

The merger rate of BBH depends on the number of haloes since their formation takes place in haloes. This is why it depends on the HMF $\frac{dn}{dM_h}(z_f, M_h)$ integrated over the

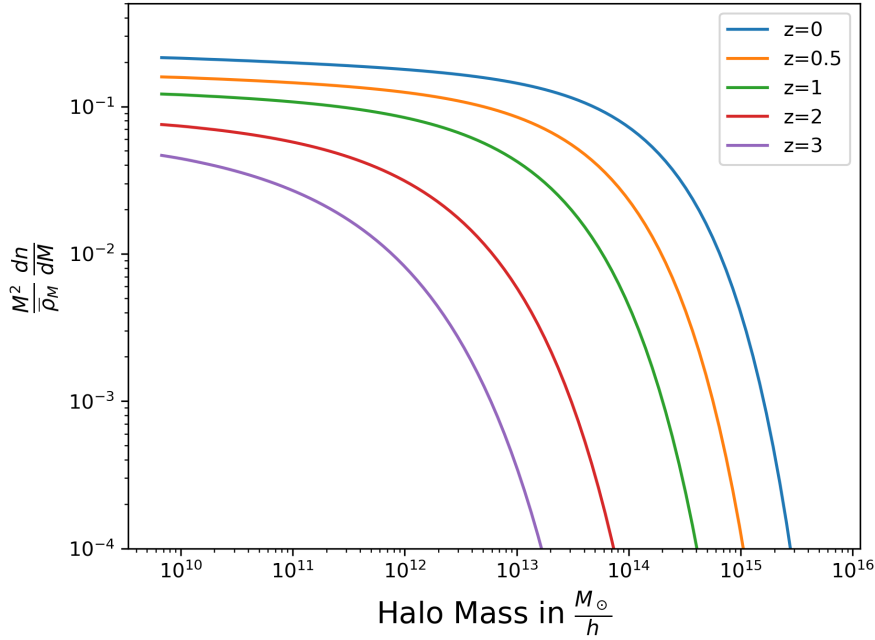


Figure 3.4: The dimensionless HMF for different redshifts z at $\Delta = 800$.

halo mass.

$$R_{BBH}(z) \propto \int dM_h \frac{dn}{dM_h}(z_f, M_h) \langle SFR(M_h, z_f) \rangle_{SF} \quad (3.19)$$

The HMF is the comoving number density of haloes with masses between M and $M + dM$. We first consider the variance of the matter density field σ^2 which we get from the linear matter power spectrum integrated over the wavenumber k with a window function. This is the Fourier transform of a tophat function in real space with the width R , corresponding to the radius of the spherical halo. Physically, overfull regions in the universe gravitationally attract and form haloes.

$$\sigma^2(R, z) = \int_0^\infty k^2 P_{lin}(k, z) W^2(k, R) dk \quad (3.20)$$

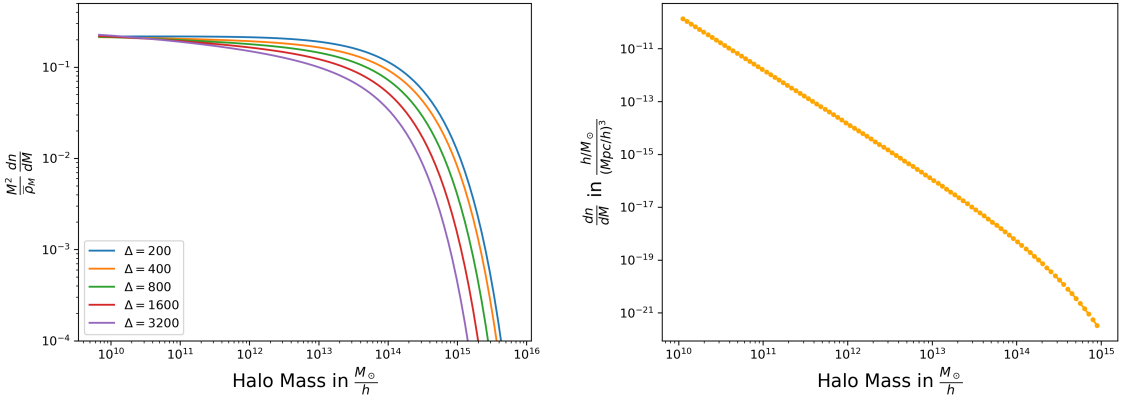
For a spherical halo model, we get the radius through the mass and the density.

$$R = \sqrt[3]{\frac{3M}{4\pi\rho_m}} \quad (3.21)$$

In the so-called peak-background-split formalism, the HMF comes from the logarithmic derivative of σ^{-1} by the halo mass.

$$\frac{dn(M)}{dM} = \frac{\rho_m}{M^2} \frac{d \ln(\frac{1}{\sigma})}{d \ln M} f_{NL}(\sigma) \quad (3.22)$$

The factor f_{NL} accounts for non-linear effects in the halo collapse. There are different ways to model these effects. A common analytical one is the Press-Schechter formalism parametrised by the critical overdensity δ_c .



(a) The dimensionless HMF for different overdensity parameters Δ at $z = 0$.
 (b) The HMF in units of $\frac{h/M_\odot}{(Mpc/h)^3}$ or respectively $\frac{h^4}{M_\odot Mpc^3}$ with $\Delta = 800$, here at $z = 0$.

Figure 3.5: The HMF at $z = 0$.

$$\delta = \frac{\delta\rho}{\bar{\rho}} \quad (3.23)$$

$$f_{PS}(\sigma) = \sqrt{\frac{2}{\pi}} \frac{\delta_c}{\sigma} \exp\left(-\frac{\delta_c^2}{2\sigma^2}\right) \quad (3.24)$$

Here, we use instead the parametrisation by Tinker et al. 2008. They use a fitting formula depending on the overdensity Δ . The overdensity characterises how much denser the sphere is compared to the average universe density $\bar{\rho}_m$ at the corresponding redshift.

$$\Delta = \frac{3M_\Delta}{4\pi R_\Delta^3 \bar{\rho}_m} \quad (3.25)$$

The non-linear corrections then have the following form.

$$f_{NL}(\sigma) = A \left(\left(\frac{\sigma}{b} \right)^{-a} + 1 \right) \exp\left(-\frac{c}{\sigma^2}\right) \quad (3.26)$$

The fitting parameters A, a, b and c functionally depend on the overdensity.

$$A = \begin{cases} 0.1(\log_{10} \Delta) - 0.05 & \Delta < 1600 \\ 0.26 & \Delta \geq 1600 \end{cases}$$

$$a = 1.43 + (\log_{10} \Delta - 2.3)^{1.5} \quad (3.27)$$

$$b = 1.0 + (\log_{10} \Delta - 1.6)^{-1.5} \quad (3.28)$$

$$c = 1.2 + (\log_{10} \Delta - 2.35)^{1.6} \quad (3.29)$$

To show how the redshift influences the dimensionless HMF $M^2 / \rho_M dn/dM$, we vary the parameter in Fig. 3.4. We can see that there are consistently more haloes

at lower z . This is consistent with the fact that structures are growing linearly with the scale factor a . In Fig. 3.5a, the overdensity parameter Δ is varied. For higher overdensities, we get a lower HMF since it is rarer for such a high overdensity to exist as a fluctuation. In our implementation, we choose a medium overdensity of $\Delta = 800$ and evaluate the HMF at different redshifts and halo masses. The HMF is shown in regular dimensions $\frac{h/M_\odot}{(Mpc/h)^3}$ for $\Delta = 800$ and $z = 0$ in Fig. 3.5b.

3.3 Star Formation Rate

The BBH merger rate also depends on the SFR which is the rate at which gas and dust are turned into stars. This is relevant since BH are end products of stellar evolution.

$$R_{BBH}(z) \propto \int dM_h \frac{dn}{dM_h}(z_f, M_h) \langle SFR(M_h, z_f) \rangle_{SF} \quad (3.30)$$

To model the SFR, we use the UNIVERSEMACHINE code from Behroozi et al. 2019. They use observational constraints and data from simulations to compute SFR for individual galaxies.

In the Λ CDM cosmology, galaxies form at the centre of haloes. Haloes are gravitationally self-bound structures that contain virialised dark matter. This means that the virial equation applies in this case. Here, T is the potential energy and U is the kinetic energy.

$$2T = U \quad (3.31)$$

So far, there exists no framework in which we can derive the SFR from first principles. The authors have found that a double power law plus Gaussian is well suited to fit the data. They then determine the best-fit parameters for this functional form. This determines the SFR for every halo at a given redshift. They use weak priors and observational constraints for less bias and the potential to reveal new physics.

To obtain the fit, they use dark matter simulations, here Bolshoi-Planck [A. A. Klypin, Trujillo-Gomez, and Primack 2011] and MultiDark Planck 2 (MDPL2) [A. Klypin et al. 2016], which simulate a mock universe. They contain halo merger trees, which can be compared to observations. Behroozi et al. used data from multiple experiments, such as the Sloan Digital Sky Survey (SDSS) [Abazajian et al. 2009] and Ultravista [McCracken et al. 2012]. The observables include stellar mass functions, UV luminosity functions and galaxy auto-correlation functions. Using this data, they compute a likelihood and run a Markov Chain Monte Carlo (MCMC) algorithm to sample the SFR range.

Like in Dall’Armi, Ricciardone, and Bertacca 2022, we consider only star-forming galaxies. This omits the fraction of quenched galaxies $f_Q = 1 - f_{SF}$, also modeled in UNIVERSEMACHINE. The adopted SFR functional form is the following.

$$\langle SFR_{SF}(M_{peak}(v_{Mpeak,z}), z) \rangle = \epsilon \left[(v^\alpha + v^\beta)^{-1} + \gamma \exp\left(-\frac{\log_{10}(v)^2}{2\delta^2}\right) \right] \quad (3.32)$$

The velocity v is defined as the ratio of the real (v_{Mpeak}) and the characteristic velocity (V) at the halo peak mass, both in km s⁻¹.

$$v = \frac{v_{Mpeak}}{V \cdot \text{km s}^{-1}} \quad (3.33)$$

The fit parameters $V, \epsilon, \alpha, \beta$ and γ depend on the rotational velocity at peak halo mass v_{Mpeak} and on the redshift. The median v_{Mpeak} depends on the halo mass and is taken from the *Bolshoi-Planck* DM simulation as:

$$v_{Mpeak}(M_h, a) = 200 \frac{\text{km}}{\text{s}} \left[\frac{M_h}{M_{200kms}(a)} \right]^3 \quad (3.34)$$

$$M_{200kms}(a) = \frac{1.64 \cdot 10^{12} M_\odot}{\left(\frac{a}{0.378}\right)^{-0.142} + \left(\frac{a}{0.378}\right)^{-1.79}}. \quad (3.35)$$

The characteristic SFR in $M_\odot \text{ yr}^{-1}$ is the global factor ϵ . For the slope of the $SFR - v_{Mpeak}$ relation, we have a faint-end and a massive-end slope parameter α and β , respectively. This is because $v_{Mpeak} \propto M_h^3$ (3.34), so a higher velocity at the peak mass corresponds to a higher halo mass. Furthermore, γ is the strength and δ the width of the Gaussian SFR efficiency boost.

The other parameters, except for δ , scale differently for different redshift regions. For V, ϵ and α , the scaling is separated into $z = 0, z \approx 1 - 2, z = 3 - 7$ and $z > 7$. The parameters β and γ have three scaling regions instead of four, as they are not well constrained at high redshifts. Here, a is the scale factor.

$$\log_{10}(V) = V_0 + V_a(1-a) + V_{la}\ln(1+z) + V_z z \quad (3.36)$$

$$\log_{10}(\epsilon) = \epsilon_0 + \epsilon_a(1-a) + \epsilon_{la}\ln(1+z) + \epsilon_z z \quad (3.37)$$

$$\alpha = \alpha_0 + \alpha_a(1-a) + \alpha_{la}\ln(1+z) + \alpha_z z \quad (3.38)$$

$$\beta = \beta_0 + \beta_a(1-a) + \beta_z z \quad (3.39)$$

$$\log_{10}(\gamma) = \gamma_0 + \gamma_a(1-a) + \gamma_{la}\ln(1+z) + \gamma_z z \quad (3.40)$$

$$\delta = \delta_0 \quad (3.41)$$

The SFR with the best-fit parameters from UNIVERSEMACHINE (not listed here, see Behroozi et al. 2019) is plotted in Fig. 3.6 as a function of v_{Mpeak} for different redshifts. As a caveat, the SFR at higher redshift is not physical at masses above the peak. In that redshift region, there are no haloes at such high masses present.

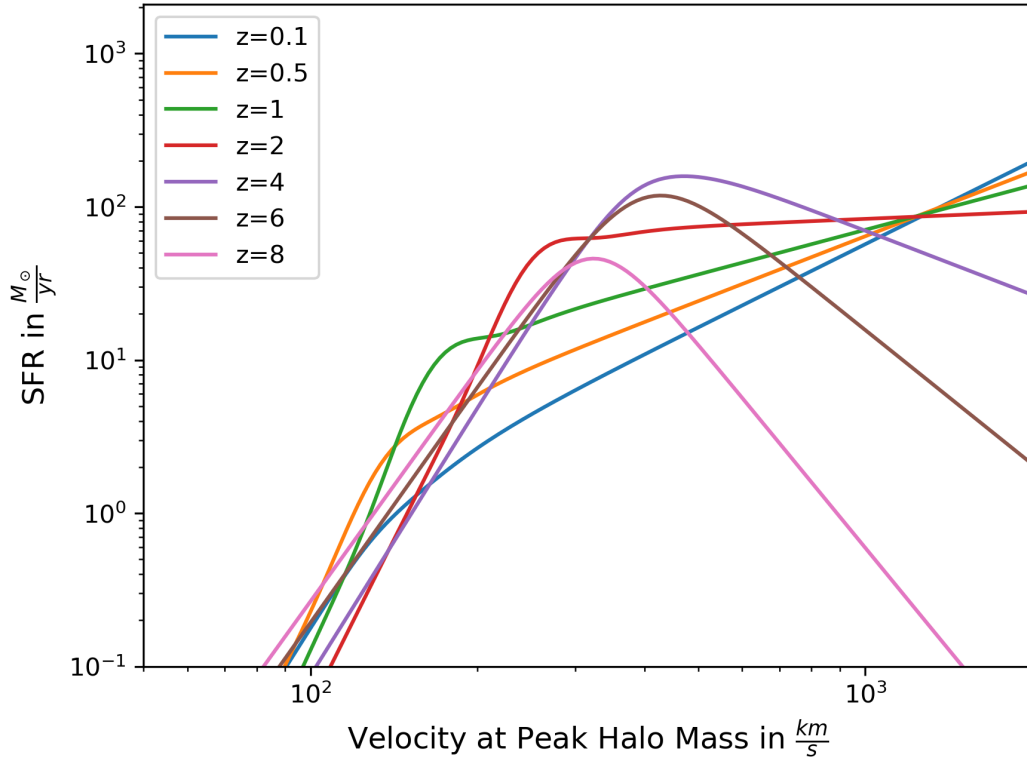


Figure 3.6: The SFR for star-forming galaxies for different redshifts. The velocity at the historical peak halo mass corresponds to the standard halo mass, see equation 3.34.

3.4 Merger Rate

With the SFR and the HMF, we can now calculate the BBH merger rate by integrating over the halo mass.

$$R_{BBH}(z) = \mathcal{A}_{LIGO}^{BBH} \int dt_d p(t_d) \int dM_h \frac{dn}{dM_h}(z_f, M_h) \langle SFR(M_h, z_f) \rangle_{SF} \quad (3.42)$$

As mass integration limits, we choose $3 \cdot 10^{11} - 4 \cdot 10^{12}$ for numerical stability. The merger rate also depends on the time delay distribution $p(t_d)$, where the time delay takes place between the formation and the merger of the binary.

$$p(t_d) = \ln \left(\frac{t(z)}{t_{d,min}} \right) \frac{1}{t_d} \quad (3.43)$$

The minimum time delay is 50 Myr, like in Dall'Armi, Ricciardone, and Bertacca 2022. The merger rate is also multiplied by a normalisation factor \mathcal{A}_{LIGO}^{BBH} , corresponding to the local merger rate estimated by LIGO and Virgo [The LIGO Scientific

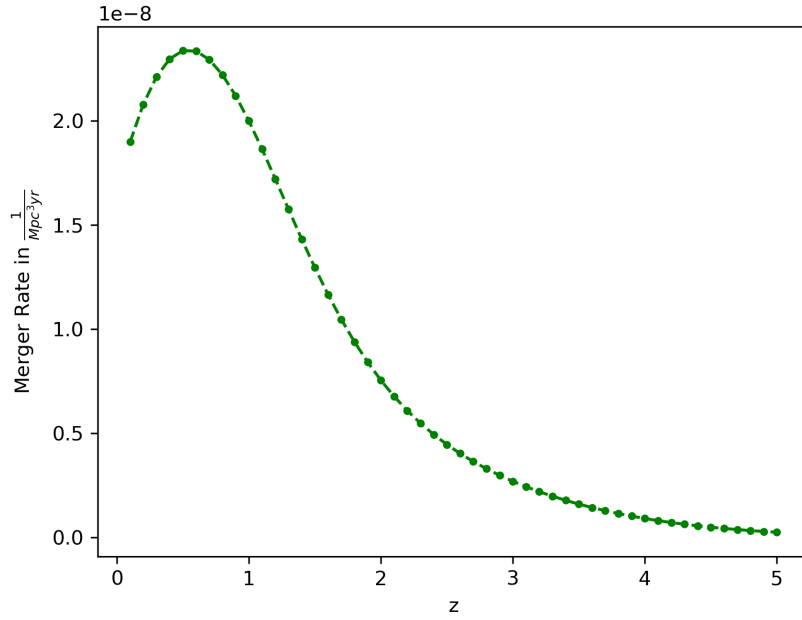


Figure 3.7: The BBH merger rate as a function of the redshift z .

Collaboration et al. 2022].

$$R_{BBH}(0) = 19 \frac{1}{\text{Gpc}^3 \text{yr}} \quad (3.44)$$

Using the results of the last sections, we calculate the BBH merger rate as a function of z , shown in Fig. 3.7.

3.5 Window Function

In Dall’Armi, Ricciardone, and Bertacca 2022, we see that the frequency dependence of the dipole comes from the evolution bias and the window function. The evolution bias accounts for the fact that more sources are created with time. The window function is used when we integrate the source functions over the redshift. It weights different redshift regions of the source functions Δ_{AGWB} from the projection effects in Section 2.2.4 depending on which ones are important for the observable, in this case, GW.

$$\delta_{AGWB}(f_o, \hat{n}) \equiv \frac{\Omega_{AGWB}(f_o, \hat{n}) - \bar{\Omega}_{AGWB}(f_o)}{\bar{\Omega}_{AGWB}(f_o)} \quad (3.45)$$

$$= \int dz \tilde{W}(f_o, z) \Delta_{AGWB}(f_o, \hat{n}, z) \quad (3.46)$$

In the standard version without frequency dependence, we can already see the influence of the different window functions and redshift ranges.

Different window functions are plotted in Fig. 3.8, namely a tophat, a Gaussian and a Dirac window. The window function determines which part of our source function we count for the density contrast. In the case of a Dirac distribution, we count all parts and skip the integration. This is why that window function leads to a higher angular power spectrum.

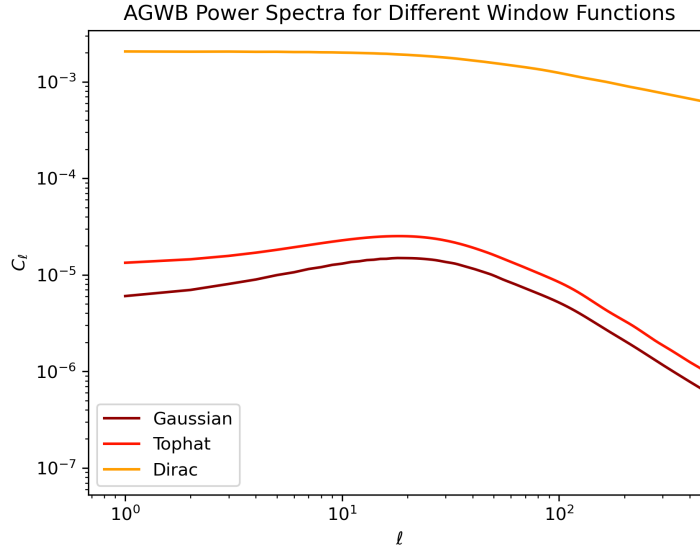


Figure 3.8: GW angular power spectrum for different window functions.

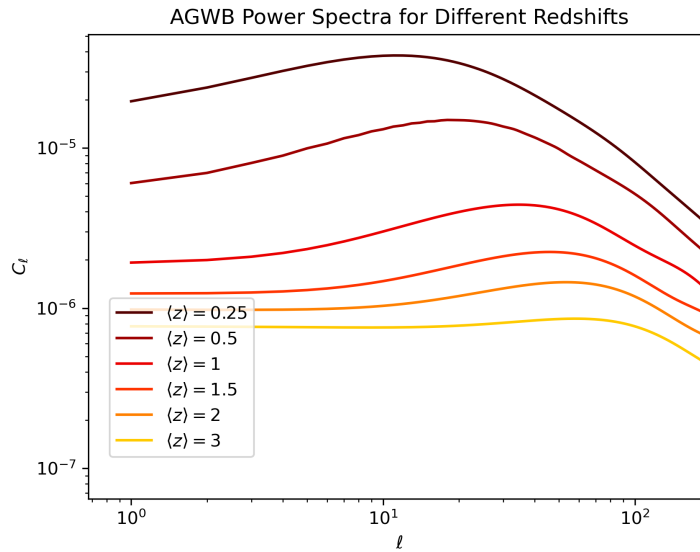


Figure 3.9: GW angular power spectrum for different redshifts.

We can see the GW angular power spectrum for different redshifts in Fig. 3.9. The anisotropies are higher for smaller redshifts. This is due to the fact that we have

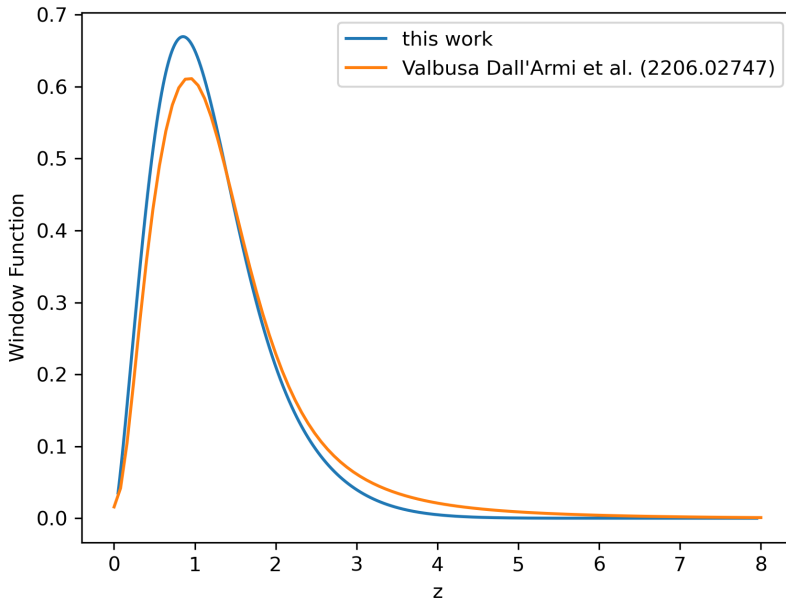


Figure 3.10: The final window function at 1 Hz for this code in blue for comparison with Dall’Armi, Ricciardone, and Bertacca 2022 in orange.

more GW sources at lower redshifts due to structure formation growing linearly with the scale factor a (neglecting the effect of dark energy).

$$\tilde{W}(z, f_0) = \frac{f_0}{\rho_c c^2 \bar{\Omega}_{AGWB}(f_0)} \frac{R_{BBH}(z)}{(1+z)H(z)} \left. \frac{dE_{GW}}{df_e d\Omega_e}(f_e) \right|_{f_e=(1+z)f_0} \quad (3.47)$$

The window function is normalised using the monopole, which is the same expression integrated over z .

$$\bar{\Omega}_{AGWB}(f_0) = \frac{f_0}{\rho_c} \frac{d\rho_{GW}}{df} \quad (3.48)$$

$$= \frac{f_0}{\rho_c c^2} \int \frac{dz}{(1+z)H(z)} R_{BBH}(z) \frac{dE_{GW}}{df_e d\Omega_e}(f_e) \quad (3.49)$$

This can in principle be modified by a detector window function depending on various physical parameters, like mass or inclination angle.

We then Fourier and Legendre transform the GW density contrast to get Legendre polynomials corresponding to multipoles on the sphere.

$$\delta_X(f_0, \vec{k}) = \int \frac{d^3 \vec{x}}{(2\pi)^{\frac{3}{2}}} \delta_X(f_0, \vec{x}) e^{i\vec{k}\vec{x}} \quad (3.50)$$

$$\Delta_l(k, f_0) = \int d\phi \int d\mu \mathcal{P}_l(\mu) \delta(\vec{k}, f_0) \quad (3.51)$$

From that, we can calculate the angular power spectrum using the primordial

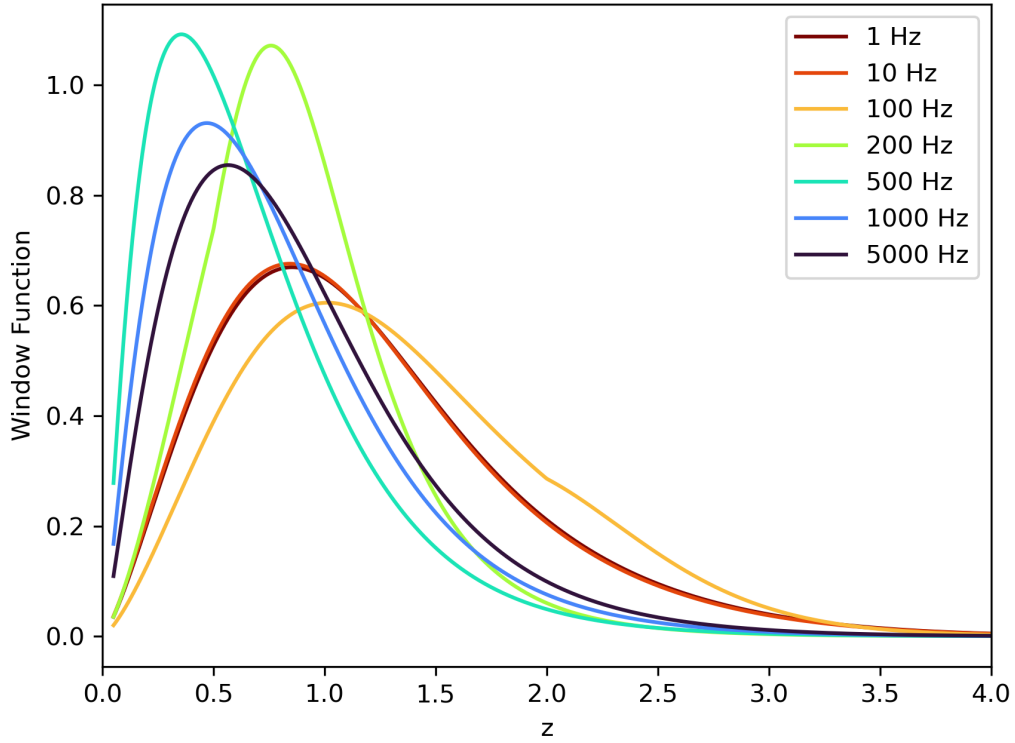


Figure 3.11: The window functions at different observed frequencies.

power spectrum.

$$C_l = 4\pi \int \frac{dk}{k} P(k) \Delta_l \Delta_l^* \quad (3.52)$$

Note, that this Δ is not the same as in equation 3.46.

In Fig. 3.10, we compare our computed window function with Dall’Armi, Ricciardone, and Bertacca 2022. Our result has a more pronounced peak and decreases quicker with redshift compared to the reference. This is the reason why the angular power spectra are different in the Result Section 6. One reason for the difference is likely the fact that we assume merger masses of $20M_\odot$ for each BH while the reference samples a probability distribution which is more physically accurate.

The window function for different frequencies from 1 to 5000 Hz is plotted in Fig. 3.11. We see that the peak shifts to lower redshifts when going from 1 Hz up to 500 Hz and then shifts to higher redshifts for frequencies above that. This will also be visible in the final angular power spectra later.

3.6 Bias & Magnification Bias

If we see GW as a tracer of the underlying dark matter density field, we have to introduce a bias for this tracer, where δ is again the density contrast.

$$\delta_{DM} = b_{GW} \delta_{GW} \quad (3.53)$$

Scelfo et al. 2018 find this bias to be 1.81 considering BH from the end-point of stellar evolution (as opposed to primordial BH).

Another bias we consider is the magnification bias. It accounts for gravitational lensing which increases the area of the source and thus decreases the observed number density. Furthermore, fainter objects can reach the magnitude threshold due to gravitational lensing.

If one compares the contributions to Δ_l^{AGWB} between `CLASSgal` and the Dall'Armi, Ricciardone, and Bertacca 2022 paper, the magnification bias has to be $s = \frac{2}{5}$ for the expressions to match. Bertacca et al. 2020 derive their expressions from first principles without introducing the magnification bias separately and obtain the result of Dall'Armi, Ricciardone, and Bertacca 2022.

3.7 Evolution Bias

The evolution bias accounts for the creation of new sources. This is why it depends on the redshift derivative of the merger rate and the energy spectrum of one merger. It enters in the projection effects in Section 2.2.4.

We can write this in terms of the logarithmic derivative of the GW energy flux with respect to the scale factor a .

$$b_e(f_0, z) = \frac{d \ln(F)}{d \ln(a)}(f_0, z) \quad (3.54)$$

$$= -\frac{1+z}{F(f_0, z)} \frac{dF}{dz}(f_0, z) \quad (3.55)$$

The energy flux of GW is a product of the energy spectrum of one binary, using the waveform by Ajith et al. 2011 and the merger rate of BBH as a function of redshift.

$$F(f_0, z) = R_{BBH}(z) \frac{dE_{GW}}{df_e d\Omega_e}(f_0, z) \quad (3.56)$$

In Fig. 3.12, we show the computed angular power spectrum with and without the evolution bias. We can see that it barely influences the overall power spectrum. Computationally, it takes much longer to consider it since the merger rate and energy spectrum are computed again at every step. The merger rate for example contains an integral over the halo mass which increases the runtime. Because of this minor influence, we neglect the evolution when computing the angular power spectra, but it can easily be activated and deactivated in the `Multi_CLASS` initialisation file (`disable_gw_evo_bias`).

Now that we modelled the window function and the GW, we can calculate the frequency-dependent angular power spectra which will be discussed later in the results section 6.1.

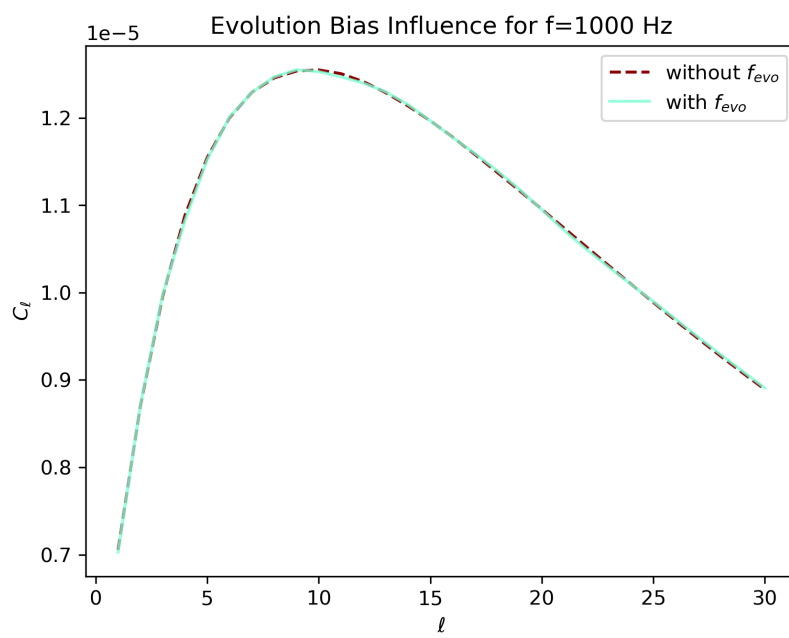


Figure 3.12: The influence of the evolution bias on the angular power spectrum at an observed frequency of 1000 Hz.

4

Instrumental Noise

Currently, the main problem in extracting the GW background is the high instrumental noise. Ground-based detectors today, like LIGO, Virgo & KAGRA are not able to detect any GW background as discussed in Section 2.2.1. This is why we need future detectors such as ET or CE to achieve a higher sensitivity. We need to assume a noise angular power spectrum to use for the separation from our computed AGWB angular power spectrum. This will be modeled after current design sensitivities of future detectors.

4.1 LIGO, Virgo & KAGRA

The current most sensitive GW observatory is LIGO in the United States, operating an interferometer with two arms, each 4 km long. The data is analysed jointly with the Virgo detector in Italy and KAGRA in Japan. This is very useful since it allows cross-correlation which lowers the noise level.

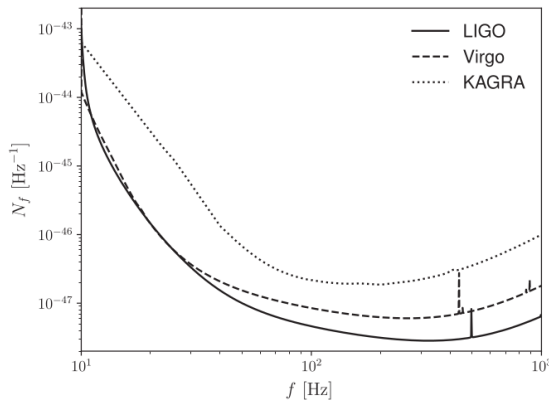


Figure 4.1: Noise sensitivity curves for the LVK detector network. For LIGO, this is the advanced LIGO A+ design sensitivity and for Virgo the O5 sensitivity. This figure is taken from Alonso et al. 2020.

In Fig. 4.1, we see how the sensitivity changes with respect to the frequency. The most sensitive frequency range is at 100 – 1000 Hz. The noise power spectrum in Fig.

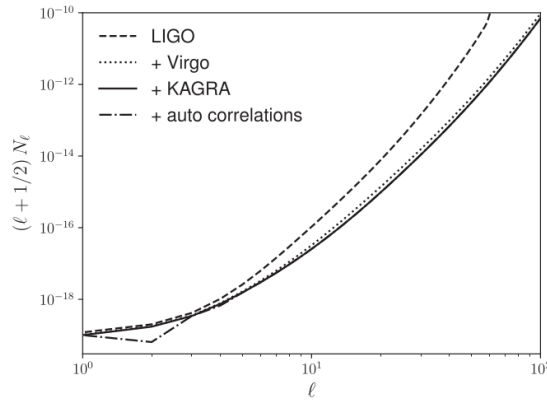


Figure 4.2: The noise angular power spectrum for LVK.

[4.1](#) tells us at which magnitude we could expect to measure a certain multipole. As can be seen in Fig. [4.2](#), using cross-correlations between the ground-based detectors improves the sensitivity, especially at higher multipoles. Adding auto-correlations of the detectors mostly influences $\ell = 2$, which is due to the L-shaped geometry of the detectors.

The sensitivity of LVK is not good enough to detect the AGWB angular power spectrum as we computed it. For this reason, we consider the next generation detectors ET and CE.

4.2 Einstein Telescope & Cosmic Explorer

ET will be a third-generation ground-based observatory, built either in the Limburg region in the Netherlands or in Sardinia, Italy. Its sensitivity will be vastly improved compared to LVK. This is due to the fact that it will operate in three arms with 10 km each instead of two arms measuring 4 km like LVK. A similar project is planned in the United States, called Cosmic Explorer (CE). It will have two arms with an unprecedented length of 40 km. The frequency sensitivity curves are shown in Fig. [4.3](#). It is sensitive in a broader frequency range than LVK, ranging from around 10 to 10^4 Hz which matches the frequency range that we consider in our angular power spectra.

ET and CE in cross-correlation will improve the sensitivity in the angular power spectrum by around 4 orders of magnitude, see Fig. [4.4](#). Here again, the improvement coming from the auto-correlation at $\ell = 2, 4$ is due to the detector shape.

Using the cross-correlations between ET and CE, see Fig. [4.4](#), the noise angular power spectrum is expected to drop from 10^{-19} to $\approx 6 \cdot 10^{-24}$ for the dipole $\ell = 1$. We will use this value to model Gaussian instrumental noise in our separation method.

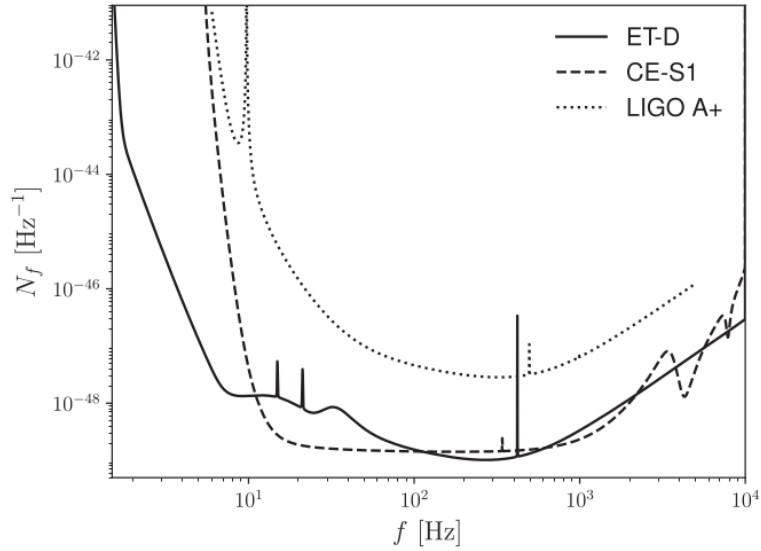


Figure 4.3: The design sensitivity curve for ET and CE compared to LIGO A+. This figure is taken from Alonso et al. 2020.

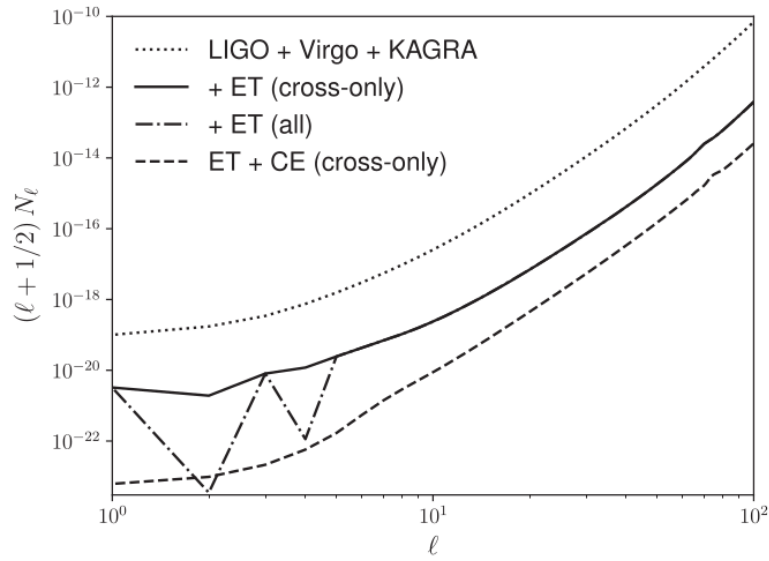


Figure 4.4: The noise angular power spectrum for different detectors at a reference frequency of 63 Hz. LVK in the dotted line, ET in solid and dot-dashed lines and CE in a dashed line. This figure is taken from Alonso et al. 2020.

5

Information Field Theory

Since the noise in GW detectors is high compared to the GW background, it requires powerful methods to separate the signal from the noise. One promising method is IFT which is a technique for signal reconstruction and field inference designed by Torsten Enßlin and his group at the Max Planck Institute in Garching [Enßlin 2013](#). Its goal is to use a formalism from Bayesian statistics and quantum field theory to be able to reuse methods to infer fields from data. The problem at the base is that we want to infer a spatially continuously distributed field from a finite amount of data. To do that, we can add our knowledge about physical laws, statistics, etc. of the problem, in the form of correlation functions.

5.1 Information Hamiltonian

If we assume a linear measurement, our data consists of the signal modified by a response function and added noise.

$$d = Rs + n \quad (5.1)$$

$$(Rs)_i = \int dx R_{ix} s_x \quad (5.2)$$

The response corresponds to the point spread function of our instrument and other linear operations performed on the data. It is reasonable to assume a linear response from our detector, see e.g. [Sathyaprakash and Schutz 2009](#). They derive an expression for the return time of the laser signal in the interferometer derived by time. The response function of the detector depends on the return time. This is proportional to the time derivative of the strain (in plus polarisation) which corresponds to our signal.

$$\frac{dt_{return}}{dt} = 1 + \sin^2(\theta) L \dot{h}_+(t) \quad (5.3)$$

Here, θ is the angle between the beam direction and the detector plane and L is

the arm length of the detector. With Gaussian noise, we get the following likelihood:

$$P(d|s) = \mathcal{N}(d - Rs, N). \quad (5.4)$$

This is a normal distribution centred around the noise $n = d - Rs$ with the noise covariance N which needs to be modelled. Using Bayes theorem, we can now calculate a posterior $P(s|d)$.

$$P(s|d) = \frac{P(d|s)P(s)}{P(d)} \quad (5.5)$$

The likelihood and the prior can be rewritten in terms of what is called an information Hamiltonian.

$$= \frac{e^{-\mathcal{H}(d,s)}}{Z_d} \quad (5.6)$$

Z_d is the partition function, which is the evidence in this case.

$$Z_d = P(d) \quad (5.7)$$

$$\mathcal{H}(d, s) = -\ln(P(d|s)) - \ln(P(s)) \quad (5.8)$$

This translates the Bayesian framework to a statistical field theory framework and allows us to use methods from (quantum) field theory to manipulate the data.

5.2 Wiener Filter

For a Gaussian prior and a Gaussian signal, we obtain the following Hamiltonian.

$$\mathcal{H}(d, s) = \frac{1}{2}(d - Rs)^\dagger N^{-1}(d - Rs) + \frac{1}{2}s^\dagger S^{-1}s \quad (5.9)$$

We need to assume a detector response R , a noise covariance N of the detector and a signal covariance S coming from physical laws. Here the signal covariance comes from the calculated angular power spectrum and the noise covariance depends on which noise we assume. The noise will be based on detector sensitivities from Chapter 4.

With quadratic completion, we can rewrite this in canonical form.

$$\mathcal{H}(d, s) = \frac{1}{2}(s - m)^\dagger D^{-1}(s - m) \quad (5.10)$$

When applying the covariance to the source, we get the mean according to the Wiener filter.

$$m = Dj \quad (5.11)$$

$$D = (S^{-1} + R^\dagger N^{-1} R)^{-1} \quad (5.12)$$

$$j = R^\dagger N^{-1} d \quad (5.13)$$

The covariance can also be written with the signal and the mean:

$$D = \langle (s - m)(s - m)^\dagger \rangle_{s|d} \quad (5.14)$$

The posterior of the Wiener filter is a Gaussian distribution with mean $s - m$ and the earlier-mentioned covariance.

$$P(s|d) = \mathcal{N}(s - m, D) \quad (5.15)$$

From this posterior, we can draw sample distributions and compare how well they match the realised signal, as we will see in the separation results section 6.

5.3 1D Toy Model

The methods of IFT are implemented in a `python` package called **NIFTy** for Numerical Information Field TheorY [Selig et al. 2013]. To show how the **NIFTy** code works in principle, we will reconstruct a one-dimensional power spectrum. From this input, a random realisation of data points is drawn from which the signal is reconstructed. The reconstruction and the residual plot are shown in Fig. 5.1. In this case, the reconstruction works quite well.

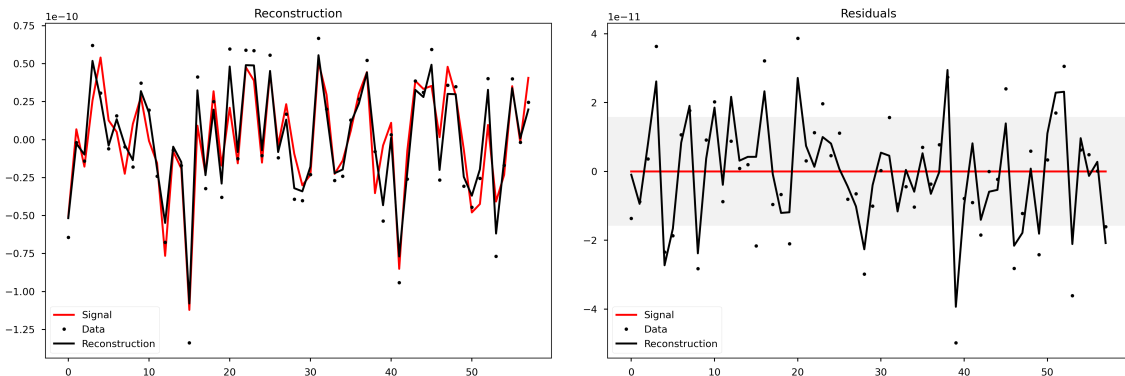


Figure 5.1: An example of using the **NIFTy** code to reconstruct an input power spectrum.

In Fig. 5.2, we show different power spectra, i.e. the input, the one from the randomly drawn signal and the reconstruction. The reconstruction power spectrum is very similar to the signal one in this toy model.

We can see that the algorithm works well in this one-dimensional toy model. In the next chapter, we will apply it to a sky map of AGWB anisotropies.

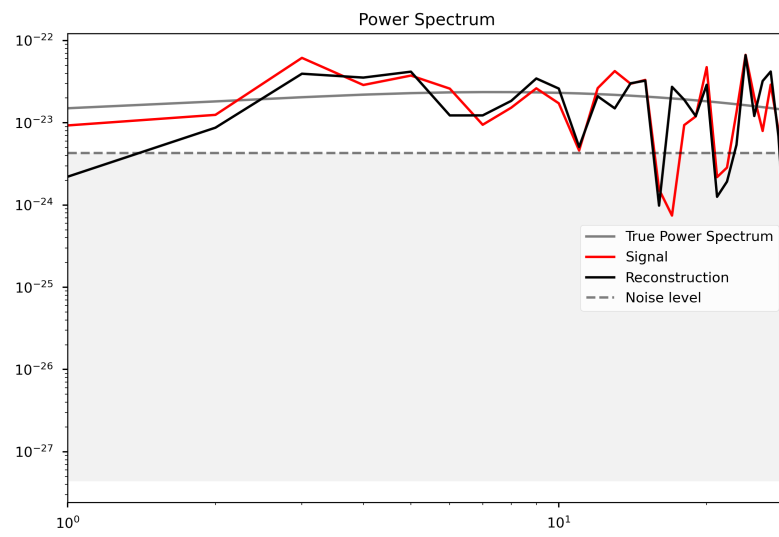


Figure 5.2: The power spectra of the one-dimensional toy model. The input power spectrum is shown in grey, the signal realisation in red and the reconstruction using IFT in black.

6

Results

To get a frequency-dependent angular power spectrum from `Multi_CLASS`, we implemented a frequency-dependent window function (see 3.5) and evolution bias (see 3.7). Using this, we can choose a measured GW frequency as an input parameter and compute the angular power spectrum. We extended the `Multi_CLASS` code to also include the dipole $l = 1$ since the standard code starts at the quadrupole $l = 2$.

6.1 Frequency Dependent AGWB Angular Power Spectrum

In Fig. 6.1, the AGWB angular power spectra are plotted for different observed frequencies. The maximum multipole calculated here is $\ell = 30$ which is relatively high for GW detectors, see 4.4. The noise power spectrum increases similarly at all multipoles, so the cutoff is slightly arbitrary. Using our formalism in `Multi_CLASS`, it is easy to calculate the anisotropies up to arbitrary high multipoles, only taking linearly more computation time. The frequency range here goes from 10 to 10,000 Hz. However, as noted in Section 2.2.1, the approximation to neglect neutron star mergers is not valid going much above 1000 Hz.

There is a clear frequency dependence of the angular power spectra ranging around one and a half orders of magnitude. We can see that the highest angular power spectrum occurs at 400 Hz while the lowest is at 100 Hz. If we focus on the dipole $l = 1$, we can plot it as a function of frequency, see Fig. 6.3b. The shape loosely resembles the energy spectrum in Fig. 3.2 which also peaks at around 400 Hz and has a minimum at around 100 Hz. The window function depends on frequency through this energy spectrum multiplied by f and divided by the monopole. Since the frequency dependence of the anisotropies comes from the window function it would make sense that this carries over.

$$\tilde{W}(z, f_o) \propto \frac{dE_{GW}/(df_e d\Omega_e)(f_e)}{\int dz (1+z)^{-1} H(z)^{-1} R_{BBH}(z) dE_{GW}/(df_e d\Omega_e)(f_e)} \quad (6.1)$$

To compare our results, we use Dall’Armi, Ricciardone, and Bertacca 2022 and their frequency-dependent dipole in Fig. 6.3. They additionally computed the kinematic dipole coming from our observer velocity with respect to the rest frame of

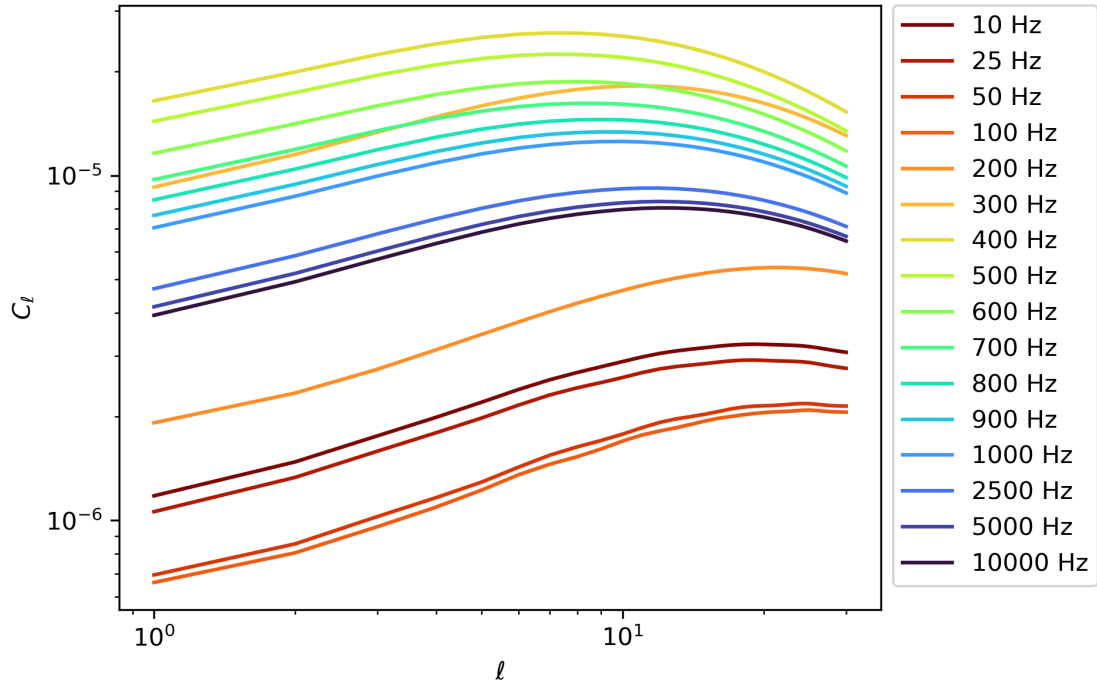


Figure 6.1: AGWB angular power spectrum of different observed frequencies, going up to $l = 30$.

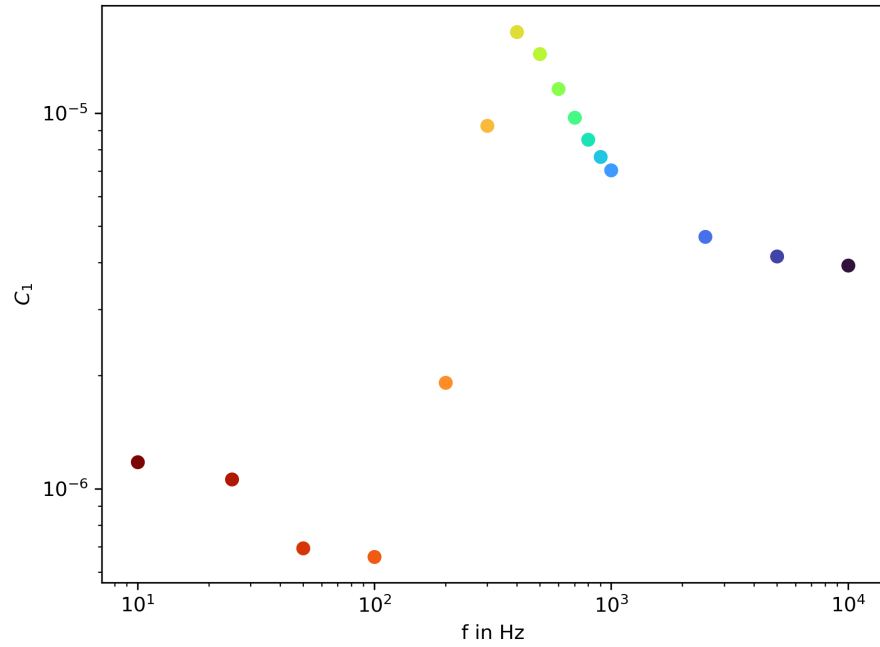


Figure 6.2: The dipole of the AGWB at different observed frequencies from 1 to 10,000 Hz.

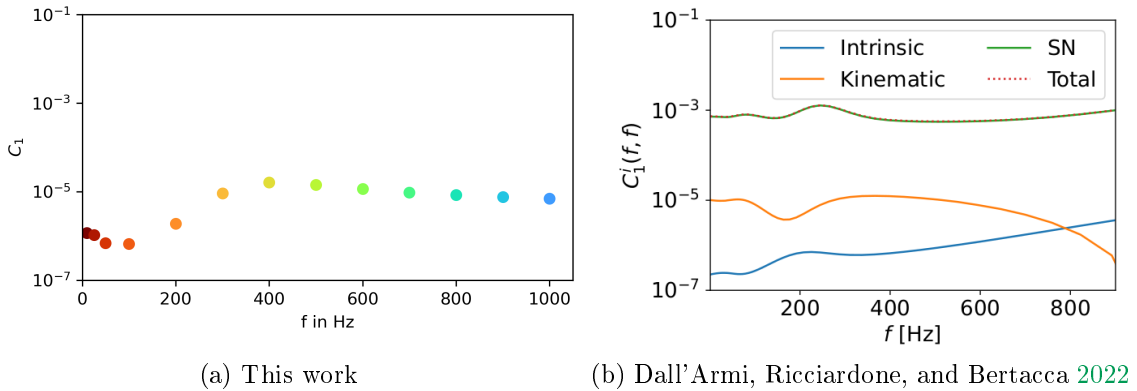


Figure 6.3: Comparison of the computed dipole contribution. On the left are the computed anisotropies using our formalism for the intrinsic anisotropies. On the right, the computed dipole by Dall’Armi, Ricciardone, and Bertacca 2022. The intrinsic dipole is shown in blue, the kinematic dipole in orange and the shot noise for the dipole in green.

the large scale structure. Furthermore, they considered the shot noise. This is the variance from a Poisson distribution which the GW mergers follow. We compare our intrinsic anisotropies with theirs in blue. The rough shape of our calculation looks similar, reaching a minimum at ≈ 100 Hz, then peaking and declining again. In their plot, the peak is at ≈ 200 Hz which is a lower frequency than ours. Additionally, they observe a continuous exponential increase for frequencies above ≈ 400 Hz. In this work, that increase is not present. Even at higher frequencies up to 10,000 Hz (see Fig. 6.3b) the dipole does not increase. Physically, to populate higher frequencies, mergers need a lower chirp mass M_c . An increasing spectrum would then mean that lower mass binaries have a higher dipole anisotropy than heavier binaries.

6.2 AGWB vs. Noise

To compare to the noise levels in Section 4.2, we have to keep in mind that we calculated relative C_l with respect to the monopole. This is because we start with the density contrast in Section 3.5.

$$\delta_{AGWB}(f_o, \hat{n}) = \frac{\Omega_{AGWB}(f_o, \hat{n}) - \bar{\Omega}_{AGWB}(f_o)}{\bar{\Omega}_{AGWB}(f_o)} \quad (6.2)$$

$$= \int dz \tilde{W}(f_0, z) \Delta_{AGWB}(f_0, \hat{n}, z) \quad (6.3)$$

Since the anisotropies are a two-point correlation, they depend quadratically on the source functions which come from the density contrast above.

$$C_l = 4\pi \int \frac{dk}{k} P(k) \Delta_l \Delta_l^* \quad (6.4)$$

Thus, to compute the physical angular power spectrum, we need to divide by the squared monopole over the solid angle.

$$C_l^{rel} = C_l \frac{(4\pi)^2}{\Omega_{GW}^2} \quad (6.5)$$

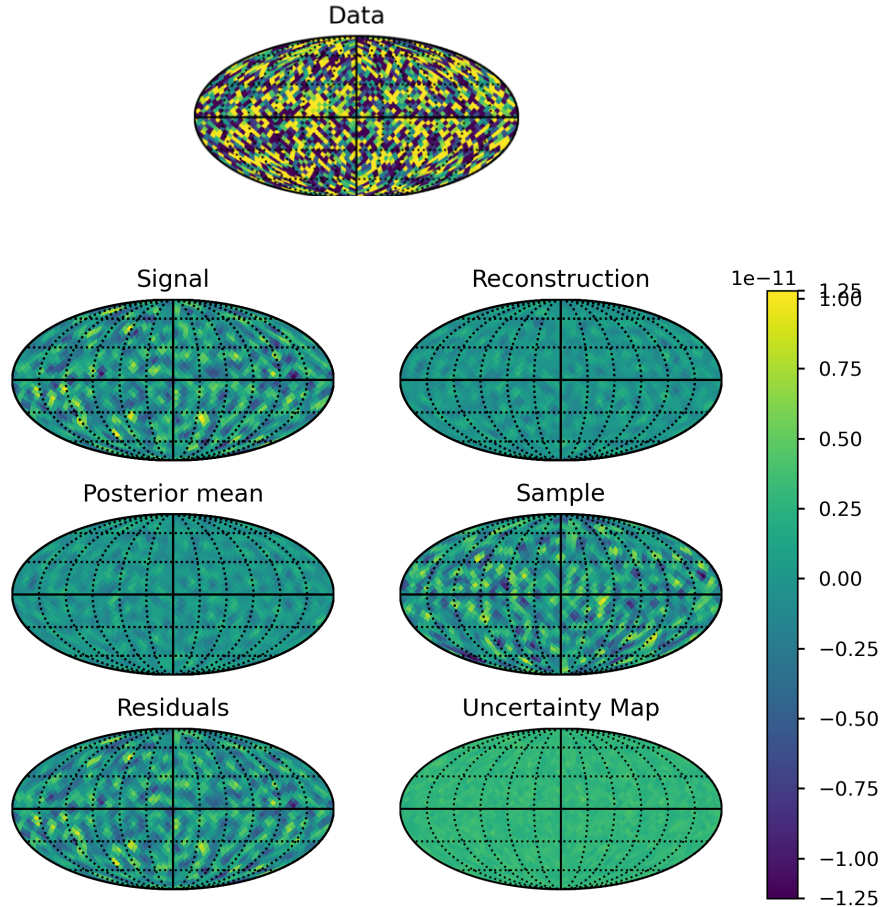


Figure 6.4: Reconstruction of the AGWB at 100 Hz on a sky map using the NIFTy code. The data on top is generated from the signal which is a realisation of the input power spectrum. The posterior mean is calculated using a Wiener filter. A sample of this is drawn randomly. The residuals represent the difference between signal and reconstruction from the first row. The uncertainty map shows the calculated errors on the reconstruction.

For the noise angular power spectrum, we assume Gaussian noise using the best anisotropic noise sensitivity for ET and CE cross-correlations (at $l = 1$). This is an optimistic assumption. The computed C_l used for the separation reach up to $l = 30$. Looking at Fig. 4.4, our assumed noise curve would have the shape of $l + \frac{1}{2}$ up to $l = 30$, which would increase more slowly than the actual sensitivity curve.

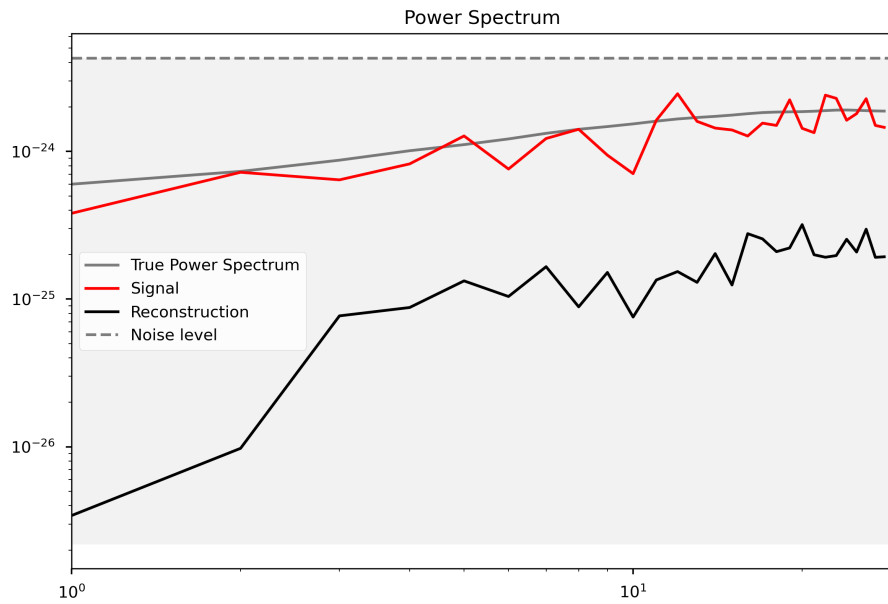


Figure 6.5: The power spectra of the AGWB separation at 100 Hz. The input power spectrum is shown in grey, the signal realisation in red and the reconstruction using IFT in black.

As seen in Fig. 6.1, we compute the lowest angular power spectrum at a frequency of 100 Hz. To test the separation in this case, we use it as input for a reconstruction on a sky map using HEALPix[Gorski et al. 2005]. At this frequency, the separation is not successful. We see that the noise in the data in Fig. 6.4 is higher than the original signal. The posterior mean and the reconstruction are both close to zero. Thus, the sample also does not mimic the signal and the residuals have the same order of magnitude as the original signal.

In the power spectrum in Fig. 6.5, we can see that the noise is roughly one order of magnitude higher than the input power spectrum which explains why a separation is not possible. The reconstruction is much lower. By trying to filter out the noise, the signal gets filtered out as well in this case. To successfully separate the signal at 100 Hz, we would need a detector that is around 2 orders of magnitude better in sensitivity compared to ET+CE.

The AGWB has the highest angular power spectrum at 400 Hz in our calculation (see Fig. 6.1). So, we use this frequency to perform another IFT separation. In the separation in Fig. 6.6, the data resembles the signal more closely than for 100 Hz. Comparing the signal to the reconstruction sky map, we see that most maxima and minima are recovered successfully. The posterior mean from the Wiener filter also mimics the signal map. When a sample is drawn from this posterior, it has some more pronounced minima and maxima but still follows the signal. However, our residuals have the same order of magnitude as the signal which is reflected in the uncertainty map as well.

In this case, the noise is half an order of magnitude lower than our power spectrum at 400 Hz which is why the reconstruction is relatively successful, see Fig. 6.7.

Regardless, the reconstruction is lower at all scales compared to the signal. If the detectors had a sensitivity of half or one order of magnitude lower, this reconstruction would be very feasible at 400 Hz.

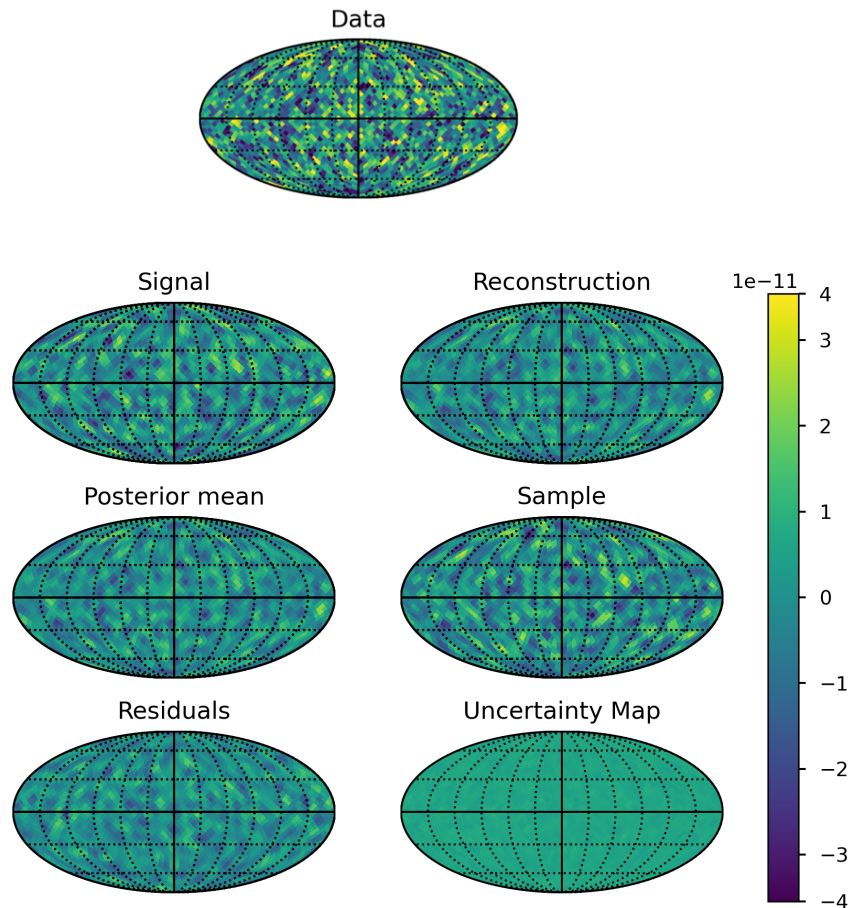


Figure 6.6: Reconstruction of the AGWB at 400 Hz on a sky map using the NIFTy code. The data on top is generated from the signal which is a realisation of the input power spectrum. The posterior mean is calculated using a Wiener filter. A sample of this is drawn randomly. The residuals represent the difference between signal and reconstruction from the first row. The uncertainty map shows the calculated errors on the reconstruction.

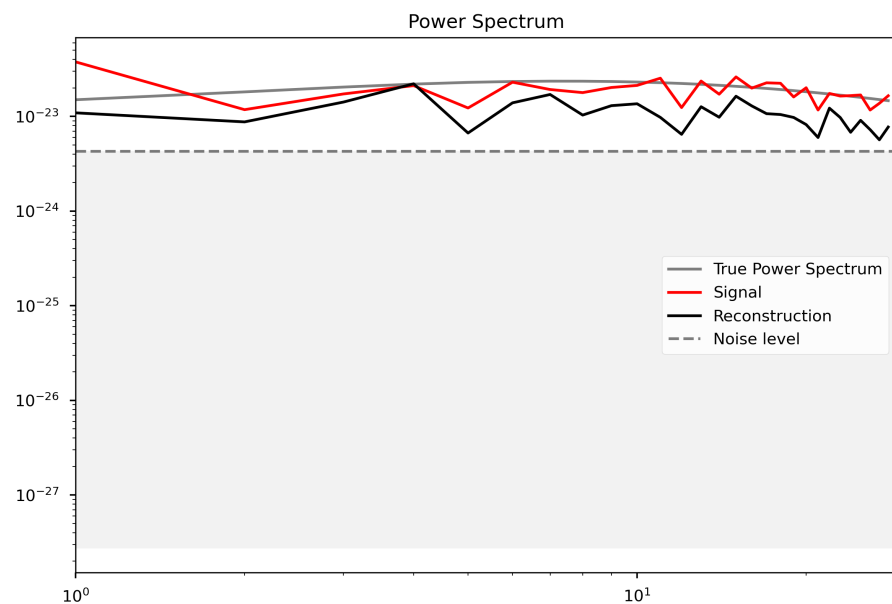


Figure 6.7: The power spectra of the AGWB separation at 400 Hz. The input power spectrum is shown in grey, the signal realisation in red and the reconstruction using IFT in black.

6.3 CGWB vs. Noise

Ideally, we could also detect the cosmological GW background with future experiments. To see how feasible this is, we use the `GW_CLASS` code by Schulze et al. 2023 that is also based on `CLASS`.

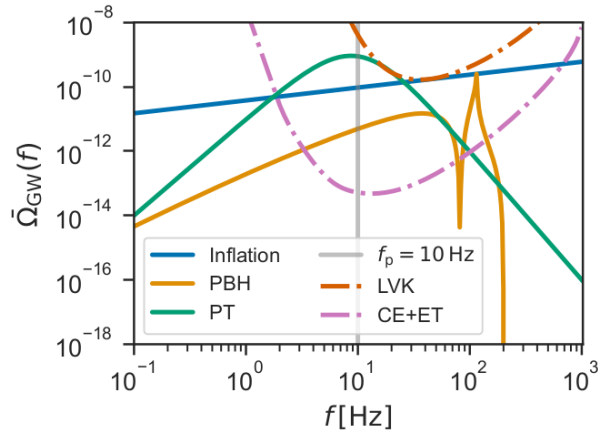


Figure 6.8: Frequency dependence of the monopole of the cosmological GW background for different generation mechanisms. The inflation scenario is shown in blue, primordial BH in orange and GW from phase transitions in green. The sensitivities for LVK and ET+CE are also shown for the monopole background.

We assume a cosmological GW background coming only from inflation, see Section 2.2.2. This has a blue tilt, meaning the background increases with frequency. To see the frequency dependency, we can look at the monopole amplitude shown in Fig. 6.8.

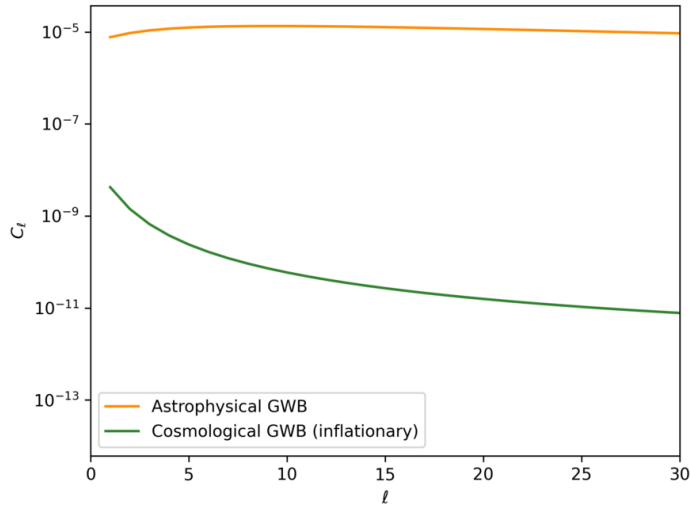


Figure 6.9: A comparison of the angular power spectra of the astrophysical versus the inflationary cosmological GW background at 900 Hz.

Due to the blue tilt, we use a high frequency of 900 Hz to test the IFT separation.

We can compare this to the AGWB at the same frequency, see Fig. 6.9. The AGWB is two to three orders of magnitude higher depending on the multipole.

The assumed noise is the same as for the AGWB case. Again, the relative C_ℓ are converted into physical C_ℓ .

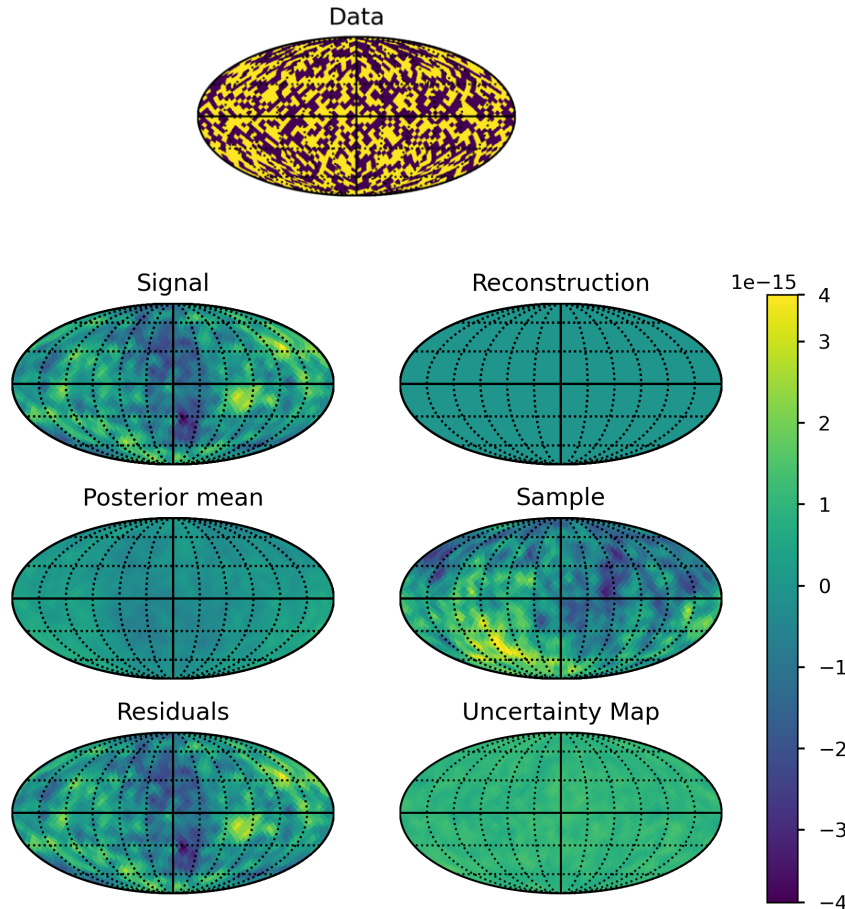


Figure 6.10: Reconstruction of the CGWB at 900 Hz on a sky map using the NIFTY code. The data on top is generated from the signal which is a realisation of the input power spectrum. The posterior mean is calculated using a Wiener filter. A sample of this is drawn randomly. The residuals represent the difference between signal and reconstruction from the first row. The uncertainty map shows the calculated errors on the reconstruction.

In Fig. 6.10 it is visible that the data is much noisier than the signal computed from the cosmological power spectrum which was expected since the cosmological background is much smaller than the AGWB. The reconstruction is thus not possible and the reconstructed sky map and the posterior mean are near zero. The sample drawn from the posterior mean does not resemble the signal and the uncertainty map averages much higher than the reconstruction.

Looking at the power spectrum in Fig. 6.11, we see that the noise level is roughly

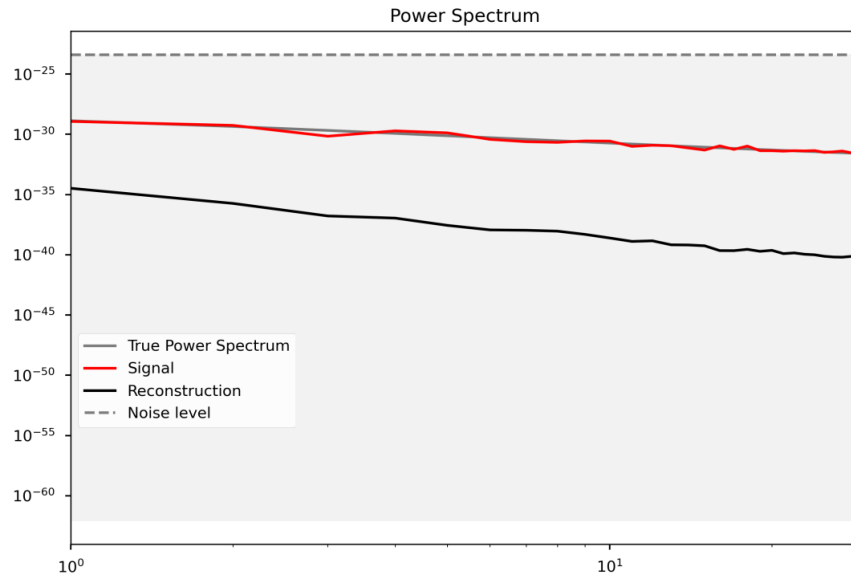


Figure 6.11: The power spectra of the CGWB separation at 900 Hz. The input power spectrum is shown in grey, the signal realisation in red and the reconstruction using IFT in black.

five orders of magnitude higher than the input and signal. Like for the AGWB at 100 Hz, the reconstruction is much lower than the signal, because it is filtered out together with the noise.

To summarise, the reconstruction was partly successful for the highest computed power spectrum (at 400 Hz) but for most frequencies, the ET+CE noise was too high to extract a signal. Naturally, this is also the case for the cosmological background since it is even lower. However, we can use this framework to input any power spectrum and model any noise to see which combinations allow fruitful reconstructions to see which backgrounds could be detectable at a given sensitivity.

Conclusion & Outlook

The goal of this work was to compute frequency-dependent AGWB anisotropies and forecast whether or not a network of next-generation ground-based GW detectors could measure the AGWB. We used the resulting angular power spectra in an IFT separation with respect to a Gaussian noise at ET+CE levels.

To do that, we considered the stochastic GW background of BBH using the number density distribution from `Multi_CLASS`. For frequencies up to around 1000 Hz, mergers containing neutron stars are negligible compared to BBH, which is why we only consider BBH in this formalism. The `Multi_CLASS` code was modified to compute the frequency-dependent angular power spectra of the AGWB. The frequency dependence comes from the window function which weights projection effects at different redshifts. These projection effects stem from the line of sight integration and include redshift space distortions, density fluctuations, the Doppler and further general relativity effects.

The window function depends on the BBH merger rate and the energy spectrum of one binary system. We consider all three phases of binary coalescence, i.e. inspiral, merger and ringdown. For the merger rate, we model the SFR since BH come from stellar evolution. We also parametrise the HMF to arrive at the merger rate. A further frequency dependence comes from the evolution bias. However, this is negligible in the final power spectrum. For the noise, we use design sensitivities of ET cross-correlated with CE using scale-independent Gaussian noise as an approximation.

Afterwards, we use the resulting anisotropies for an IFT separation with the `NIFTy` package. The separation does not work for a lower angular power spectrum at 100 Hz but works roughly for a higher one at 400 Hz. To test the same method with the cosmological GW background, we use `GW_CLASS` assuming an inflationary background at 900 Hz. Since this background is below the astrophysical one, the reconstruction is not possible.

Apart from the instrumental noise, the kinematic dipole and statistical shot noise also obscure the intrinsic AGWB. In the future, those can be modelled using the same formalism and can then be included in the IFT separation. The instrumental noise can also be modelled in a scale-dependent way to be more realistic, i.e. increasing at higher multipoles.

Furthermore, astrophysical parameters, like the mass of each merging BH and the inclination angle, could be drawn from a physical probability distribution. The

framework can also be extended to consider neutron star mergers.

Computing one angular power spectrum at a frequency is still computationally costly at the moment. Improving the speed of the implementation would also allow computing more frequencies to see the full frequency dependence. It would then be interesting to use the functional frequency dependence directly in `NIFTy`. This should improve the separation since it is an extra dimension that can be used in IFT. Using more powerful IFT methods other than the Wiener filter would help extract precise information from an eventual data set as well. The next step would then be separating the AGWB from the cosmological one, either without or in the presence of instrumental noise.

With a well-modeled AGWB we can hope to have a detection using next or next-to-next generation GW detectors. This would tell us more about the properties and sources of this background and shine light on the cosmological principle.

Acknowledgements

Firstly, I would like to thank my supervisors Prof. Dr. Philipp Mertsch and Prof. Dr. Julien Lesgourgues. Lorenzo Valbusa Dall'Armi also offered his expertise on gravitational waves as well as on the used formalism and he kindly provided some of his data to compare with my code. Additionally, Sefa Pamuk, Tobias Thrien and Christian Radermacher were always happy to discuss physical concepts with me and provide help regarding the CLASS code. Laurin Söding helped me with some concerns regarding the NIFTy code which was very useful. Special thanks also to Julia, Nikolas, Sefa, Tobias, Clemens, Nikhil, Ankit and my parents for proofreading.

Lastly, I want to thank my parents for always supporting me and all the other Master students for the nice discussions and the good time throughout this year.

Bibliography

- Planck Collaboration et al. (Oct. 2016). “*Planck* 2015 results: IX. Diffuse component separation: CMB maps”. In: *Astronomy & Astrophysics* 594, A9. ISSN: 0004-6361, 1432-0746. DOI: [10.1051/0004-6361/201525936](https://doi.org/10.1051/0004-6361/201525936). URL: <http://www.aanda.org/10.1051/0004-6361/201525936> (visited on 08/10/2023).
- Agazie, Gabriella et al. (June 28, 2023). *The NANOGrav 15-year Data Set: Evidence for a Gravitational-Wave Background*. DOI: [10.3847/2041-8213/acdac6](https://doi.org/10.3847/2041-8213/acdac6). arXiv: [2306.16213\[astro-ph, physics:gr-qc\]](https://arxiv.org/abs/2306.16213). URL: <http://arxiv.org/abs/2306.16213> (visited on 09/15/2023).
- Bellomo, Nicola et al. (Oct. 6, 2020). “Beware of commonly used approximations I: errors in forecasts”. In: *Journal of Cosmology and Astroparticle Physics* 2020.10, pp. 016–016. ISSN: 1475-7516. DOI: [10.1088/1475-7516/2020/10/016](https://doi.org/10.1088/1475-7516/2020/10/016). arXiv: [2005.10384\[astro-ph\]](https://arxiv.org/abs/2005.10384). URL: <http://arxiv.org/abs/2005.10384> (visited on 08/10/2023).
- Blas, Diego, Julien Lesgourgues, and Thomas Tram (July 1, 2011). “The Cosmic Linear Anisotropy Solving System (CLASS) II: Approximation schemes”. In: *Journal of Cosmology and Astroparticle Physics* 2011.7, pp. 034–034. ISSN: 1475-7516. DOI: [10.1088/1475-7516/2011/07/034](https://doi.org/10.1088/1475-7516/2011/07/034). arXiv: [1104.2933\[astro-ph\]](https://arxiv.org/abs/1104.2933). URL: <http://arxiv.org/abs/1104.2933> (visited on 09/15/2023).
- Holten, J. W. van (Mar. 2019). “Gravitational waves from generalized newtonian sources”. In: *Fortschritte der Physik* 67.3, p. 1800083. ISSN: 00158208. DOI: [10.1002/prop.201800083](https://doi.org/10.1002/prop.201800083). arXiv: [1809.05670\[astro-ph, physics:gr-qc\]](https://arxiv.org/abs/1809.05670). URL: <http://arxiv.org/abs/1809.05670> (visited on 09/11/2023).
- Christensen, Nelson (Jan. 1, 2019). “Stochastic gravitational wave backgrounds”. In: *Reports on Progress in Physics* 82.1, p. 016903. ISSN: 0034-4885, 1361-6633. DOI: [10.1088/1361-6633/aae6b5](https://doi.org/10.1088/1361-6633/aae6b5). URL: <https://iopscience.iop.org/article/10.1088/1361-6633/aae6b5> (visited on 08/10/2023).
- Abbott, R. et al. (July 23, 2021). “Upper limits on the isotropic gravitational-wave background from Advanced LIGO and Advanced Virgo’s third observing run”. In: *Physical Review D* 104.2, p. 022004. ISSN: 2470-0010, 2470-0029. DOI: [10.1103/PhysRevD.104.022004](https://doi.org/10.1103/PhysRevD.104.022004). URL: <https://link.aps.org/doi/10.1103/PhysRevD.104.022004> (visited on 10/17/2023).
- Phinney, E. S. (Aug. 1, 2001). *A Practical Theorem on Gravitational Wave Backgrounds*. arXiv: [astro-ph/0108028](https://arxiv.org/abs/astro-ph/0108028). URL: <http://arxiv.org/abs/astro-ph/0108028> (visited on 09/15/2023).
- The LIGO Scientific Collaboration et al. (Feb. 23, 2022). *The population of merging compact binaries inferred using gravitational waves through GWTC-3*. arXiv:

- 2111.03634[astro-ph, physics:gr-qc]. URL: <http://arxiv.org/abs/2111.03634> (visited on 10/04/2023).
- Capurri, Giulia et al. (Nov. 1, 2021). “Intensity and anisotropies of the stochastic Gravitational Wave background from merging compact binaries in galaxies”. In: *Journal of Cosmology and Astroparticle Physics* 2021.11, p. 032. ISSN: 1475-7516. DOI: [10.1088/1475-7516/2021/11/032](https://doi.org/10.1088/1475-7516/2021/11/032). arXiv: 2103.12037[astro-ph, physics:gr-qc]. URL: <http://arxiv.org/abs/2103.12037> (visited on 09/22/2023).
- Abbott, B. P. et al. (Feb. 11, 2016). “Observation of Gravitational Waves from a Binary Black Hole Merger”. In: *Physical Review Letters* 116.6, p. 061102. ISSN: 0031-9007, 1079-7114. DOI: [10.1103/PhysRevLett.116.061102](https://doi.org/10.1103/PhysRevLett.116.061102). URL: <https://link.aps.org/doi/10.1103/PhysRevLett.116.061102> (visited on 09/01/2023).
- Schulze, Florian et al. (May 2, 2023). *GW_CLASS: Cosmological Gravitational Wave Background in the Cosmic Linear Anisotropy Solving System*. arXiv: 2305.01602[astro-ph, physics:gr-qc]. URL: <http://arxiv.org/abs/2305.01602> (visited on 08/10/2023).
- Alonso, David et al. (June 22, 2020). “Noise angular power spectrum of gravitational wave background experiments”. In: *Physical Review D* 101.12, p. 124048. ISSN: 2470-0010, 2470-0029. DOI: [10.1103/PhysRevD.101.124048](https://doi.org/10.1103/PhysRevD.101.124048). URL: <https://link.aps.org/doi/10.1103/PhysRevD.101.124048> (visited on 08/10/2023).
- Robson, Travis, Neil Cornish, and Chang Liu (May 23, 2019). “The construction and use of LISA sensitivity curves”. In: *Classical and Quantum Gravity* 36.10, p. 105011. ISSN: 0264-9381, 1361-6382. DOI: [10.1088/1361-6382/ab1101](https://doi.org/10.1088/1361-6382/ab1101). arXiv: 1803.01944[astro-ph, physics:gr-qc]. URL: <http://arxiv.org/abs/1803.01944> (visited on 09/22/2023).
- Scelfo, Giulio et al. (Sept. 25, 2018). “GW\$\times\$LSS: Chasing the Progenitors of Merging Binary Black Holes”. In: *Journal of Cosmology and Astroparticle Physics* 2018.9, pp. 039–039. ISSN: 1475-7516. DOI: [10.1088/1475-7516/2018/09/039](https://doi.org/10.1088/1475-7516/2018/09/039). arXiv: 1809.03528[astro-ph, physics:gr-qc]. URL: <http://arxiv.org/abs/1809.03528> (visited on 08/10/2023).
- Di Dio, Enea et al. (Nov. 20, 2013). “The CLASSgal code for Relativistic Cosmological Large Scale Structure”. In: *Journal of Cosmology and Astroparticle Physics* 2013.11, pp. 044–044. ISSN: 1475-7516. DOI: [10.1088/1475-7516/2013/11/044](https://doi.org/10.1088/1475-7516/2013/11/044). arXiv: 1307.1459[astro-ph]. URL: <http://arxiv.org/abs/1307.1459> (visited on 08/09/2023).
- Dall’Armi, Lorenzo Valbusa, Angelo Ricciardone, and Daniele Bertacca (Nov. 1, 2022). “The Dipole of the Astrophysical Gravitational-Wave Background”. In: *Journal of Cosmology and Astroparticle Physics* 2022.11, p. 040. ISSN: 1475-7516. DOI: [10.1088/1475-7516/2022/11/040](https://doi.org/10.1088/1475-7516/2022/11/040). arXiv: 2206.02747[astro-ph, physics:gr-qc]. URL: <http://arxiv.org/abs/2206.02747> (visited on 02/06/2023).
- Kaiser, Nick (July 1987). “Clustering in real space and in redshift space”. In: *Monthly Notices of the Royal Astronomical Society* 227.1, pp. 1–21. ISSN: 0035-8711, 1365-2966. DOI: [10.1093/mnras/227.1.1](https://doi.org/10.1093/mnras/227.1.1). URL: <https://academic.oup.com/mnras/article-lookup/doi/10.1093/mnras/227.1.1> (visited on 10/02/2023).

- Ajith, P. et al. (June 15, 2011). “Inspiral-merger-ringdown waveforms for black-hole binaries with non-precessing spins”. In: *Physical Review Letters* 106.24, p. 241101. ISSN: 0031-9007, 1079-7114. DOI: [10.1103/PhysRevLett.106.241101](https://doi.org/10.1103/PhysRevLett.106.241101). arXiv: [0909.2867\[astro-ph, physics:gr-qc\]](https://arxiv.org/abs/0909.2867). URL: <http://arxiv.org/abs/0909.2867> (visited on 02/06/2023).
- Bardeen, James M., William H. Press, and Saul A. Teukolsky (Dec. 1972). “Rotating Black Holes: Locally Nonrotating Frames, Energy Extraction, and Scalar Synchrotron Radiation”. In: *The Astrophysical Journal* 178, p. 347. ISSN: 0004-637X, 1538-4357. DOI: [10.1086/151796](https://doi.org/10.1086/151796). URL: <http://adsabs.harvard.edu/doi/10.1086/151796> (visited on 10/03/2023).
- Maggiore, Michele (2008). *Gravitational waves*. OCLC: 262833538. Oxford: Oxford University Press. ISBN: 978-0-19-171766-6.
- Behroozi, Peter et al. (Sept. 21, 2019). “UniverseMachine: The Correlation between Galaxy Growth and Dark Matter Halo Assembly from $z=0-10$ ”. In: *Monthly Notices of the Royal Astronomical Society* 488.3, pp. 3143–3194. ISSN: 0035-8711, 1365-2966. DOI: [10.1093/mnras/stz1182](https://doi.org/10.1093/mnras/stz1182). arXiv: [1806.07893\[astro-ph\]](https://arxiv.org/abs/1806.07893). URL: <http://arxiv.org/abs/1806.07893> (visited on 02/06/2023).
- Klypin, Anatoly A., Sebastian Trujillo-Gomez, and Joel Primack (Oct. 20, 2011). “DARK MATTER HALOS IN THE STANDARD COSMOLOGICAL MODEL: RESULTS FROM THE BOLSHOI SIMULATION”. In: *The Astrophysical Journal* 740.2, p. 102. ISSN: 0004-637X, 1538-4357. DOI: [10.1088/0004-637X/740/2/102](https://doi.org/10.1088/0004-637X/740/2/102). URL: <https://iopscience.iop.org/article/10.1088/0004-637X/740/2/102> (visited on 10/02/2023).
- Klypin, Anatoly et al. (Apr. 21, 2016). “MultiDark simulations: the story of dark matter halo concentrations and density profiles”. In: *Monthly Notices of the Royal Astronomical Society* 457.4, pp. 4340–4359. ISSN: 0035-8711, 1365-2966. DOI: [10.1093/mnras/stw248](https://doi.org/10.1093/mnras/stw248). URL: <https://academic.oup.com/mnras/article-lookup/doi/10.1093/mnras/stw248> (visited on 10/02/2023).
- Abazajian, Kevork N. et al. (June 1, 2009). “THE SEVENTH DATA RELEASE OF THE SLOAN DIGITAL SKY SURVEY”. In: *The Astrophysical Journal Supplement Series* 182.2, pp. 543–558. ISSN: 0067-0049, 1538-4365. DOI: [10.1088/0067-0049/182/2/543](https://doi.org/10.1088/0067-0049/182/2/543). URL: <https://iopscience.iop.org/article/10.1088/0067-0049/182/2/543> (visited on 10/02/2023).
- McCracken, H. J. et al. (Aug. 2012). “UltraVISTA: a new ultra-deep near-infrared survey in COSMOS”. In: *Astronomy & Astrophysics* 544, A156. ISSN: 0004-6361, 1432-0746. DOI: [10.1051/0004-6361/201219507](https://doi.org/10.1051/0004-6361/201219507). URL: <http://www.aanda.org/10.1051/0004-6361/201219507> (visited on 10/02/2023).
- Tinker, Jeremy L. et al. (Dec. 2008). “Toward a halo mass function for precision cosmology: the limits of universality”. In: *The Astrophysical Journal* 688.2, pp. 709–728. ISSN: 0004-637X, 1538-4357. DOI: [10.1086/591439](https://doi.org/10.1086/591439). arXiv: [0803.2706\[astro-ph\]](https://arxiv.org/abs/0803.2706). URL: <http://arxiv.org/abs/0803.2706> (visited on 08/10/2023).
- Bertacca, Daniele et al. (May 11, 2020). “Projection effects on the observed angular spectrum of the astrophysical stochastic gravitational wave background”. In: *Physical Review D* 101.10, p. 103513. ISSN: 2470-0010, 2470-0029. DOI: [10.1103/PhysRevD.101.103513](https://doi.org/10.1103/PhysRevD.101.103513). arXiv: [1909.11627\[astro-ph, physics:gr-qc\]](https://arxiv.org/abs/1909.11627). URL: <http://arxiv.org/abs/1909.11627> (visited on 08/10/2023).

- Enßlin, Torsten (2013). “Information field theory”. In: pp. 184–191. DOI: [10.1063/1.4819999](https://doi.org/10.1063/1.4819999). arXiv: [1301.2556\[astro-ph,physics:physics,stat\]](https://arxiv.org/abs/1301.2556). URL: <http://arxiv.org/abs/1301.2556> (visited on 10/12/2023).
- Sathyaprakash, B. S. and B. F. Schutz (Dec. 2009). “Physics, Astrophysics and Cosmology with Gravitational Waves”. In: *Living Reviews in Relativity* 12.1, p. 2. ISSN: 2367-3613, 1433-8351. DOI: [10.12942/lrr-2009-2](https://doi.org/10.12942/lrr-2009-2). arXiv: [0903.0338\[astro-ph, physics:gr-qc\]](https://arxiv.org/abs/0903.0338). URL: <http://arxiv.org/abs/0903.0338> (visited on 10/17/2023).
- Selig, Marco et al. (June 2013). “NIFTY - Numerical Information Field Theory - a versatile Python library for signal inference”. In: *Astronomy & Astrophysics* 554, A26. ISSN: 0004-6361, 1432-0746. DOI: [10.1051/0004-6361/201321236](https://doi.org/10.1051/0004-6361/201321236). arXiv: [1301.4499\[astro-ph, physics:math-ph, physics:physics, stat\]](https://arxiv.org/abs/1301.4499). URL: <http://arxiv.org/abs/1301.4499> (visited on 10/18/2023).
- Gorski, K. M. et al. (Apr. 2005). “HEALPix: A Framework for High-Resolution Discretization and Fast Analysis of Data Distributed on the Sphere”. In: *The Astrophysical Journal* 622.2, pp. 759–771. ISSN: 0004-637X, 1538-4357. DOI: [10.1086/427976](https://doi.org/10.1086/427976). URL: <https://iopscience.iop.org/article/10.1086/427976> (visited on 10/16/2023).

Appendix A

Call Graph

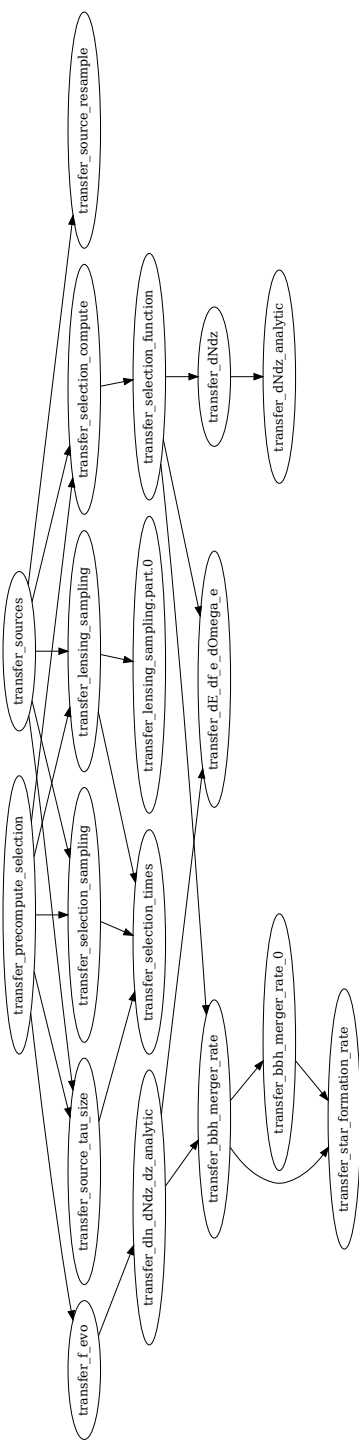


Figure A.1: The dependency graph of `transfer.c` in the modified Multi_CLASS code starting from `transfer_sources` and `transfer_precompute_selection`. The HMF is not shown, since it is located in `nonlinear.c`

List of Figures

2.1	Illustration of the plus and cross polarisations varying with time	5
2.2	The GW inspiral phase waveform	8
2.3	The GW energy density parameter as a function of frequency from 1 to 10,000 Hz	11
2.4	The different stages of a BBH merger with the corresponding waveform .	12
3.1	The three phases of a binary coalescence: inspiral, merger and ringdown .	18
3.2	The energy spectrum as a function of the observed frequency for a BBH merger where both BH have a mass of $20M_{\odot}$ at $z = 0$	20
3.3	The energy spectrum $dE_{GW,e}/df_e d\Omega_e$ at different observed frequencies as a function of redshift, again for two BH with a mass of $20M_{\odot}$ each.	21
3.4	The dimensionless HMF for different redshifts z at $\Delta = 800$	22
3.5	The HMF at $z = 0$	23
3.6	The SFR for star-forming galaxies for different redshifts	26
3.7	The BBH merger rate as a function of the redshift z	27
3.8	GW angular power spectrum for different window functions	28
3.9	GW angular power spectrum for different redshifts	28
3.10	The final window function at 1 Hz for this code for comparison with Dall’Armi, Ricciardone, and Bertacca 2022	29
3.11	The window functions at different observed frequencies	30
3.12	The influence of the evolution bias on the angular power spectrum at an observed frequency of 1000 Hz	32
4.1	Noise sensitivity with respect to frequency for LVK	33
4.2	The noise angular power spectrum for LVK	34
4.3	The design sensitivity curve for ET and CE compared to LIGO A+ .	35
4.4	The noise angular power spectrum for different detectors at a reference frequency of 63 Hz	35
5.1	An example of using the NIFTy code to reconstruct an input power spectrum	38
5.2	The power spectra of the one-dimensional toy model	39
6.1	AGWB angular power spectrum of different observed frequencies, going up to $l = 30$	41
6.2	The dipole of the AGWB at different observed frequencies from 1 to 10,000 Hz	41

6.3	Comparison of the computed dipole contribution to Dall’Armi, Ricciardone, and Bertacca 2022.	42
6.4	Reconstruction of the AGWB at 100 Hz on a sky map using the NIFTy code.	43
6.5	The power spectra of the AGWB separation at 100 Hz.	44
6.6	Reconstruction of the AGWB at 400 Hz on a sky map using the NIFTy code.	46
6.7	The power spectra of the AGWB separation at 400 Hz.	47
6.8	Frequency dependence of the monopole of the cosmological GW background for different generation mechanisms.	48
6.9	A comparison of the angular power spectra of the astrophysical versus the inflationary cosmological GW background at 900 Hz.	48
6.10	Reconstruction of the CGWB at 900 Hz on a sky map using the NIFTy code.	49
6.11	The power spectra of the CGWB separation at 900 Hz.	50
A.1	The dependency graph of <code>transfer.c</code> in the modified <code>Multi_CLASS</code> code.	59